Chapter 1

Introduction

1.1 Background

From an aerodynamic perspective, the wind flow over structures is characterized by many complex features. This can often include separating flow, reattachment, vortex formulation and shedding; and all of these in conjunction with time-varying scales. These complexities lead to significant challenges if it is desired to simulate the wind loads for the purposes of predicting the structural response of buildings and bridges. The method for addressing these problems has often depended on wind tunnel experimentation. These simulations, however, present their own shortcomings: cost, inability to establish dynamic similarity through Reynolds number matching, and the lack of a comprehensive understanding of the effects of turbulence.

In recent years however, significant advancements have made predicting wind loads on structures through computational means a realizable goal. Computing power has increased and computational methodologies have been improved, leading to the advancement of several numerical methods that accurately simulate wind loads on structures. Under different incident flow conditions, the response of structural elements such as roof sheathing panels, fasteners, and connectors have been predicted for low-rise structures. There is also the possibility for developing time-domain numerical simulations of the flow field around tall buildings and bridges.

Atmospheric flows around buildings, bridges, and other similar civil structures have intrinsically large Reynolds numbers. Given that inertial effects are typically on the order of 100,000 times that of any viscous behavior, modeling these flows is not straight

forward. Motivated by these difficulties, this thesis is concerned with the aerodynamic aspects of the wind flow over civil structures. The "Discrete Vortex Method" is offered as a reliable procedure for predicting the wind loads that develop over such objects.

1.2 CFD Tools for Modeling Wind Loads

Several computational fluid dynamics methodologies have been developed for the purposes of predicting the wind loads over large civil structures. These methods, however, yield their own shortcomings; addressing these problems is the aim of this thesis.

Although Direct Numerical Simulation, DNS, enables an accurate prediction of wind loads, it is not feasible to implement this method for the magnitude Reynolds numbers encountered with most wind engineering applications. Reynolds-Averaged Navier-Stokes (RANS) and Large Eddy Simulation (LES) have been proposed for use with these scenarios. In the case of RANS, the time-averaged Navier-Stokes and continuity equations are solved together. A statistical turbulence model is used to account for the Reynolds stresses, $\overline{u_i u_j}$, by relating them to the mean velocity gradients. Because such models do not account for history and transport effects on turbulence, they are not well-suited for complex flow regions such as flow separation. Additionally, RANS solutions require the use of wall functions to overcome erroneous predictions near walls. Such functions are not mathematically justified in the separation regimes.

In Large Eddy Simulations, the three-dimensional Navier-Stokes equations are solved numerically. Because the small turbulence scales cannot be resolved numerically at high Reynolds numbers, they are filtered out and modeled with what is usually referred to as the Sub-grid Scale (SGS) model. Again, the no-slip condition at the wall requires a very high resolution near all solid surfaces. While LES presents the best opportunity for characterizing wind loads on structures, its implementation in time-domain solutions of fluid-structure interaction problems remains an issue. This is mostly due to the CPU time required to solve all scales of the flow field.

In comparison to Navier-Stokes based computational fluid dynamics techniques, the Discrete Vortex Method (DVM), as implemented in this work, presents a unique, new opportunity for predicting wind loads over specific structures. For instance, a two-dimensional procedure could be used to quickly develop estimates for the wind loads over a bridge cross-section. These, in turn, can then be used to lay the foundations for a technique to passively control the motion of the bridge. Moreover, the ability of DVM to account for the history of the flow field makes it a potentially powerful approach for modeling the time averaged pressure along the surface of a low-rise structure.

Qin, et al. (2001) present a comparison of different aspects of DVM with respect to DNS or LES. In particular, they note

- By introducing vortex blobs at the corner and following their fate as they convect over a suitable region, the flow is described using a Lagrangian approach, instead of the Eulerian approach used when solving Navier-Stokes equations.
- There is no need to define a computational grid
- Viscous effects are assumed to be small everywhere except in the boundary layer; turbulence in the outer flow is captured by introducing vorticity into the field. This vorticity is allowed to convect from sharp corners.
- The solution presented is two-dimensional, while the real flow is three-dimensional; this is also the case with DNS and LES. Vorticity can be distributed over surfaces in three-dimensions; this would require more computer resources, as is the case again with DNS and LES.
- The vorticity modeling technique presented here does not allow for viscous dissipation, which is not the case when solving Navier-Stokes equations, which allow for the dissipation of turbulent energy.

1.3 Objectives

"Future research," Taylor et al. (1999) stated, should be "aimed at extending the validation of the DVM to a wider range of geometries relevant to the field of wind engineering, such as suspension bridge deck sections" (pp 267). This thesis aims to advance this goal with two specific applications. The first is a two-dimensional flow over a surface-mounted prism. This is a generic flow, often used to simulate the flow over low-rise structures, ship hulls, and other bluff bodies. In particular, the interest is in accurately portraying the pressure distribution over a square cross-section. In the second application, the two-dimensional flow over a bridge deck is considered. The possible use of leading and trailing edge flaps for the reduction of wind loads is explored with promising results.

Chapter 2

Discrete Vortex Method—Background and Code Development

In this chapter, the two-dimensional discrete vortex code used to obtain the results presented within this work is discussed. Following an overview of the theoretical background of the Discrete Vortex Method, the specific techniques used to develop the DVM code for the flow over a surface-mounted prism are presented. This technique is then extended for use with a bridge deck in Chapter 4.

2.1 Theoretical Background

Most computational fluid codes are developed from Navier-Stokes Equations (2.1.1); however, as discussed in the introduction, these methods often produce results that fall significantly short of reality.

$$\rho \frac{D\underline{U}}{Dt} = -\nabla \underline{p} + \mu \nabla^2 \underline{U} \qquad (2.1.1)$$

The Discrete Vortex Method, having foundations not with Navier-Stokes, but rather with the Biot-Savart Law, does not fall victim to the same problems. This is accomplished by developing the velocity field from the vorticity field. The vorticity field is generated through two discretization processes. Solid surfaces are first modeled with vorticity elements. Additionally, the vorticity generated in the boundary layer, which is then

convected into the field via separation behavior, is simulated by propagating vortex "blobs" into the computational domain.

2.1.1 The Biot-Savart Law

The focus of the Discrete Vortex Method is expressing the velocity field from the vorticity field, which is accomplished by inverting the three-dimensional definition of vorticity:

$$\underline{\omega}(\underline{r},t) = \nabla \times \underline{U}(\underline{r},t) \tag{2.1.2}$$

Under the assumption of incompressible flow, which is valid for flows over both buildings and bridges, Equation 2.1.3 holds, expressing the Continuity Equation.

$$\nabla \cdot \underline{U} = 0\,, \tag{2.1.3}$$

When the Continuity Equation is valid, the velocity vector, $\underline{U}$, can be described as the curl of some other vector, $\underline{B}$. This is demonstrated by Equation 2.1.4.

$$\underline{U} = \nabla \times \underline{B} \tag{2.1.4}$$

Because $\underline{B}$ is indeterminate to the extent of a gradient vector, $\underline{B}$ satisfies Equation 2.1.3 in similar fashion as $\underline{U}$. This relationship allows the vector identity given as Equation 2.1.5 to be simplified to Equation 2.1.6.

$$\underline{\nabla} \times (\underline{\nabla} \times \underline{B}) = \underline{\nabla}(\underline{\nabla} \cdot \underline{B}) - \nabla^2 \underline{B} \tag{2.1.5}$$

$$\nabla^2 \underline{B} = -\underline{\nabla} \times (\underline{\nabla} \times \underline{B}) \tag{2.1.6}$$

Using Equation 2.1.4 to substitute in $\underline{U}$ for its relationship to $\underline{B}$ gives Equation 2.1.7.

$$\nabla^2 \underline{B} = -\underline{\nabla} \times \underline{U} \tag{2.1.7}$$

From here, the definition of vorticity, Equation 2.1.2, gives Poisson's Equation for $\underline{B}$ in terms of the vorticity:

$$\nabla^2 \underline{B} = -\underline{\omega} \tag{2.1.8}$$

Equation 2.1.9 gives the value of $\underline{B}$ located by the vector, $\underline{r}$, as a solution to Poisson's Equation.

$$\underline{B}(\underline{r},t) = \frac{1}{4\pi} \int_{Vol} \frac{\underline{\omega}}{|\underline{r} - \underline{r}_c|} d(Vol) \tag{2.1.9}$$

In this case, $\underline{\omega} \cdot d(Vol)$ is the element of the vortex distribution located by $\underline{r}_c$. By applying Equation 2.1.4 again here, the three-dimensional Biot-Savart Law, which expresses the velocity in terms of the vorticity, can be written as

$$\underline{U} = \underline{\nabla} \times \underline{B} = \frac{1}{4\pi} curl \int_{Vol} \frac{\underline{\omega}}{|\underline{r} - \underline{r}_c|} d(Vol) \tag{2.1.10}$$

This yields:

$$\underline{U}(\underline{r},t) = \frac{1}{4\pi} \int_{Vol} \frac{\underline{\omega}(\underline{r}_c,t) \times (\underline{r} - \underline{r}_c)}{|\underline{r} - \underline{r}_c|^3} d(Vol) \tag{2.1.11}$$

For the simplest case of one vortex in two-dimensions, Figure 2.1 describes the vectoral relationships inherent to Equation 2.1.11. The velocity at a point q; located by a vector, $\underline{r}_q$; and induced by a the vortex element, $\underline{\omega}(\underline{r}_c,t)$, is given by $\underline{U}_{qc}(\underline{r}_q,t)$.

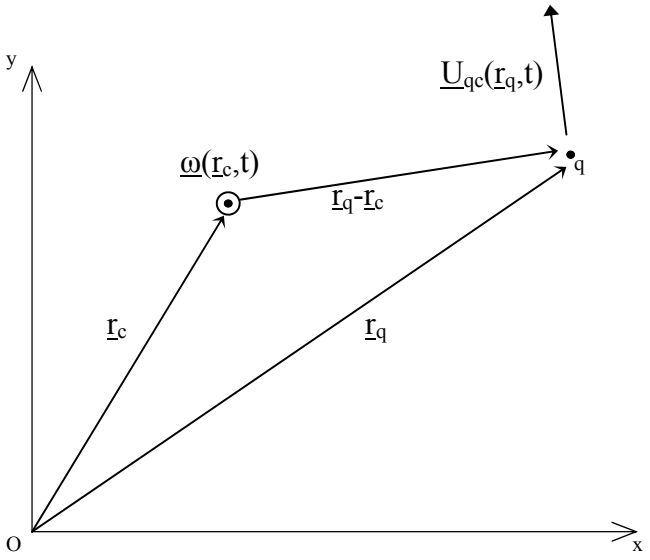

Figure 2.1: Description of Vorticity Dynamics

Summing the effects of many vortex elements with the Biot-Savart integral (Equation 2.1.11) yields a much less complicated computational procedure than solving Navier-Stokes differential equations (Taylor, Vezza 1999). The integral, which is valid over the entire vorticity-containing region, is often separated into area regions as defined by object boundaries: both outside and inside the bodies (Qin, et al. 2001).

2.1.2 Surface Vorticity Modeling

In order to generate the proper flow behavior around an object within the computational domain using Equation 2.1.11, all boundary layers are represented with a vorticity sheet (Qin, et al. 2001). This vorticity sheet is distributed in terms of a vorticity per unit length function, γ. The units of γ are vorticity per unit length, or length per unit time: the same as velocity. Consequently, the value of γ gives the velocity of the fluid at any solid surface. By modeling the solid surfaces of the body in this manner, the thickness of the boundary layer becomes infinitesimally small. This implies that a discontinuous jump in velocity occurs: from zero at the body to the potential flow outside the vorticity sheet, which would be the case for an infinite Reynolds number.

For bodies that can be sufficiently expressed in two-dimensions, the surface vorticity modeling becomes quite straight forward. A series of node points are used to break the surface of the object into panels, developing linear approximations for any curved surfaces (Taylor, Vezza 1999). The total vorticity of each panel is then defined in terms of a circulation per unit length function, γ_n. The slight increment in velocity, $d\underline{U}_b(\underline{r},t)$, due to a vorticity element with circulation per unit length, $\gamma(s(\underline{r}_c),t)$, having an incremental length, ds, can be found using the rectilinear version of the Biot-Savart Law. Where $\underline{r}$ locates the point of velocity calculation, and $\underline{r}_c$ the vorticity element, this is given by Equation 2.1.12.

$$d\underline{U}_b(\underline{r},t) = -\frac{1}{2\pi}\hat{k}\times\frac{\gamma(s(\underline{r}_c),t)\cdot(\underline{r}-\underline{r}_c)}{\left|\underline{r}-\underline{r}_c\right|^2}ds(\underline{r}_c) \tag{2.1.12}$$

Integrating along the surface of the body, the total velocity field induced by the vortex sheet representing the body, s, is given by:

$$\underline{U}_b(\underline{r},t) = -\frac{\hat{k}}{2\pi}\times\oint_C\gamma(s(\underline{r}_c),t)\cdot\frac{(\underline{r}-\underline{r}_c)}{\left|\underline{r}-\underline{r}_c\right|^2}ds(\underline{r}_c) \tag{2.1.13}$$

Typically, linear distributions of the vorticity sheet are used for each panel in order to yield a piecewise continuous definition of γ along the surface of the object. Additionally, this allows discrete values of γ to be assigned to the midpoint of each panel simply by averaging the values of the vorticity sheet at either end. By exchanging the differential length element for the actual length of each panel, δ_s, Equation 2.1.13 can be written in terms of a summation over the number of panels along the body.

$$\underline{U}_b(\underline{r},t) = -\frac{\hat{k}}{2\pi}\times\sum_{i=1}^{M}\gamma_i\delta_{s_i}\cdot\frac{(\underline{r}-\underline{r}_i)}{\left|\underline{r}-\underline{r}_c\right|^2} \tag{2.1.14}$$

2.1.3 Modeling of Boundary Layer Separation

In addition to the surface vorticity modeling technique, a second vortex discretization process must be implemented to accurately portray separation and other key wake characteristics. For real flows, the boundary layer sheds into the flow field at sharp corners as a sheet of vorticity. These vortex sheets then roll and wrap around one another, creating a scenario that is virtually impossible to manage numerically. Consequently, discrete vortices are introduced into the computational domain from any sharp corners. If these vortices are allowed to undergo convection and diffusion with the flow field, the flow develops the characteristics associated with boundary layer vorticity behavior (Qin, et al. 2001).

Unfortunately, because the stream function for point vortices, Equation 2.1.15, depends logarithmically on r, a singularity develops in the Biot-Savart Law if the vortex sheet is approximated by a series of point vortices (Munson, et al. 2002).

$$\psi = \frac{-\Gamma}{2\pi}\ln(r) \tag{2.1.15}$$

Due to this singularity, if two point vortices come too close to one another in the wake, the resulting high magnitudes of their individual stream functions cause them to undergo rapid, discontinuous convection during the next time step. To alleviate this problem, the concept of vortex "blobs" is implemented instead of point vortices (Qin, et al. 2001).

A vortex blob is created by distributing the circulation from the initial point-vortex, Γ, over a finite, circular core with a distribution function, $\zeta_\sigma(d)$.

$$\zeta_\sigma(d) = \frac{d^2}{1+d^2} \tag{2.1.16}$$

In this case, d, depends on the radius of the vortex blob, σ, and the distance from the point of calculation that the i^{th} blob is located (Qin, et al. 2001).

$$d = \frac{\left\| \underline{r}_c - \underline{r}_i \right\|}{\sigma} \tag{2.1.17}$$

Following this discretization scheme, the vorticity field, $\omega(\underline{r}_c, t)$, can be approximated by the following summation of all vortex blobs (Barba, 2005):

$$\omega(\underline{r}_c, t) = \sum_{i=1}^{N} \Gamma_i(t) \zeta_{\sigma_i}(d) \tag{2.1.18}$$

The velocity field introduced by the vortex blobs is then given by (Qin, et al. 2001)

$$\begin{aligned} \underline{U}_w(\underline{r}, t) &= \frac{1}{2\pi} \sum_{i=1}^{N} \Gamma_i(t) \zeta_{\sigma_i}(d) \cdot \hat{k} \times \frac{\underline{r} - \underline{r}_i}{\left\| \underline{r} - \underline{r}_i \right\|^2} \\ &= \frac{1}{2\pi} \sum_{i=1}^{N} \Gamma_i(t) \cdot \hat{k} \times \frac{\underline{r} - \underline{r}_i}{\left\| \underline{r} - \underline{r}_i \right\|^2 + \sigma^2} \end{aligned} \tag{2.1.19}$$

2.1.4 Satisfying the No-Penetration Boundary Condition

Qualitatively, the no-penetration boundary condition stipulates that no momentum is allowed to enter or exit the body. Quantitatively, this means that the flow must have no component normal to the boundary; the flow must be parallel to the surface of the body. Equation 2.1.20 expresses the boundary condition in terms of a dot product between the total velocity vector, $\underline{U}$, and the unit vector normal to the surface of the body.

$$\underline{U}(\underline{r}, t) \cdot \hat{n}(\underline{r}) = 0 \tag{2.1.20}$$

The total velocity vector is found through a simple super-position of the three velocity components: $\underline{U}_b$, from surface vorticity; $\underline{U}_w$, from the vortex blobs; and the free-stream velocity, $\underline{U}_\infty$ (Qin, et al. 2001).

$$\underline{U} = \underline{U}_b + \underline{U}_w + \underline{U}_\infty \qquad (2.1.21)$$

The boundary conditions described by Equation 2.1.20 are applied to Equations 2.1.14 and 2.1.19 to realize the values of γ on the surface of the body and the values of Γ for the vortex blobs. The effect of Equation 2.1.20 near the boundary is demonstrated by Figure 2.2, where the three exposed surfaces of the building are represented by a series of vortices. Because the free-stream is flowing in the positive x-direction, the clockwise vortex orientation shown ensures that the local velocity vector, $\underline{U}$, always falls parallel to the surface of the building.

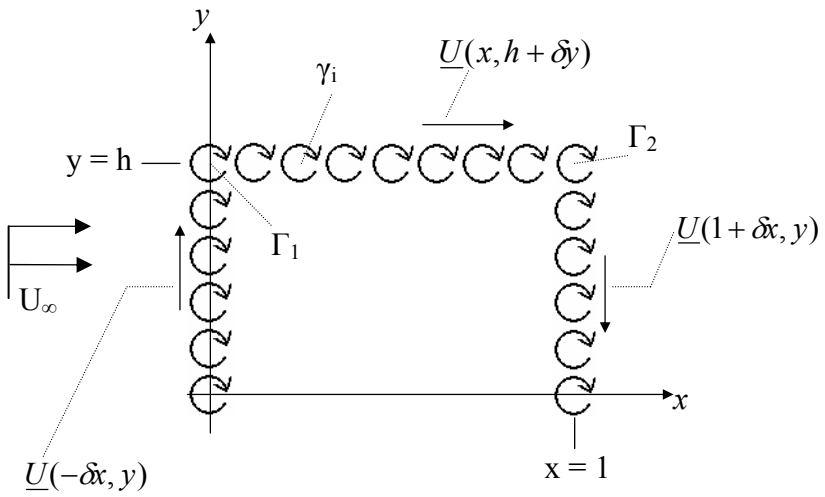

Figure 2.2: Effect of Surface Vorticity on Velocity Field

2.2 Original DVM Code: Uniform Flow over a Surface-Mounted Prism

A two-dimensional Discrete Vortex Code was developed by Qin et al. (2001) for the purpose of determining the loads that develop on the walls and roof of a surface-mounted prism. The code produced velocity magnitude and vorticity fields as well as surface pressure distributions at various times after the field reaches steady-state. The results showed that the DVM code nearly describes both the major flow characteristics as well as the resultant pressure distribution on the rectangle (Qin, et al. 2001). Some unexpected results were generated for the behavior just behind the leeward side of the prism.

In the code, a rectangle was used to represent the prism cross-section; the stream-wise dimension of the rectangle was set to one, and its non-dimensional height, 0.65. Following the procedure described in Section 2.1.2, a series of nodes was used to divide the three exposed faces of the rectangle into vorticity elements, the strength of which is not known *a priori*. Given the bluff-body characteristics of the rectangle, flow separation occurs at both top corners. In order to capture the behavior of the large gradients that develop as a consequence of this behavior, elements near the top of the prism needed to be quite small. On the other hand, the panels near the bottom of the prism can be longer because the flow structure is not as complex. Varying the panel length on the two vertical faces in this manner yields a significant savings in terms of the computational speed.

Because separation is known to occur from the two top corners of the rectangle, vortex blobs are introduced at these locations and are convected into the flow field to simulate the separating shear layer. Equations 2.1.16 and 2.1.17, which are dependent on a dimensionless length parameter, σ, govern the manner with which the vorticity of each blob is distributed. By using a value of 10^{-6} for σ, the resulting quantized vorticity field was found to sufficiently approximate a continuous vorticity sheet. In order to capture the effect of mounting the prism on a surface, a series of image vortices were used. For every vortex element, both surface panels and discrete blobs, a vortex of equal strength and opposite sign is placed below the mounting surface to create a mirror image vorticity distribution (Qin, et al. 2001).

2.2.1 Structure of the DVM code

The original code, developed by Qin et al. (2001), was written using Fortran 90 to interface with seven parallel processors. Three physical quantities normalized to a prism width of one are defined as input constants: the height of the prism, h, and the horizontal and vertical components of the free-stream velocity, v_x and v_y. For comparison purposes, however, an h value of 0.65 is used for all cases presented in this work. The code was

found to accurately resolve the flow field in an optimal time by setting the number of vortex panels on each wall, *nw*, equal to 40 and the length of each time step, Δt, to 0.001.

The first computational step of the program is to define the vorticity panels along the surface of the rectangle. With the origin defined at the lower windward corner, a series of nodes locate the end points of each panel. For illustrative purposes, Figure 2.3 presents a description of the nodal distribution using a reduced number of nodes (from 40 on the wall and 300 on the roof, to five and 20, respectively). As previously stated, the panels making up the walls are longer at the bottom than the top; a sine function is used to distribute the nodes according to

$$ynode(i) = h \cdot \sin\left(\frac{\pi}{2 \cdot nw} \cdot (i-1)\right) \tag{2.2.1}$$

where *i* varies from 1 to *nw*+1. Using the length of each element, the linear distribution of vorticity for each panel is collapsed onto one of the nodes at either end of the element. It is for this reason that each node is also referred to as "Panel Vorticity" in Figure 2.3. The manner in which the "Image Panel Vorticity" creates a reflection of the prism about the *x*-axis can also be seen in Figure 2.3.

As stated above, the no penetration boundary condition must be enforced at each panel; therefore, each panel represents one equation that must be solved to describe the flow field. To progress in time, the unknown values of vorticity must be solved so that the flow satisfies these equations. Rather than using panel vorticity unknowns at the two corners, a vortex blob is introduced into the field at these two points for each time step, representing two unknowns of a different type that must be solved along with the vorticity values from the other panels. Because a node is located at the beginning and the end of the prism surface, the number of panels is equal to the number of nodes, less one. This would suggest that the number of unknowns exceeds the number of equations; however, the vorticity is known to be zero at the first and last nodes, reducing the number of unknown γ values by two. These points of contact with the ground and are labeled

$\gamma(1)$ and $\gamma(nc+1)$ in Figure 2.3. Because of this physical constraint, the number of unknown γ values is reduced to one less than the number of panels. In order to fully constrain the system, the least energy configuration is selected.

The Kutta condition, which states that the pressure, and therefore velocity, must be constant across any sharp trailing edge, is often an important consideration. When using the Discrete Vortex Method; however, this condition is automatically satisfied. Because the velocity induced by the vortex-blobs is constant for a particular radius, the pressure is also constant. Therefore, when a vortex blob is shed from the trailing corner, it distributes the same pressure at the end of the top surface as the top of the right face.

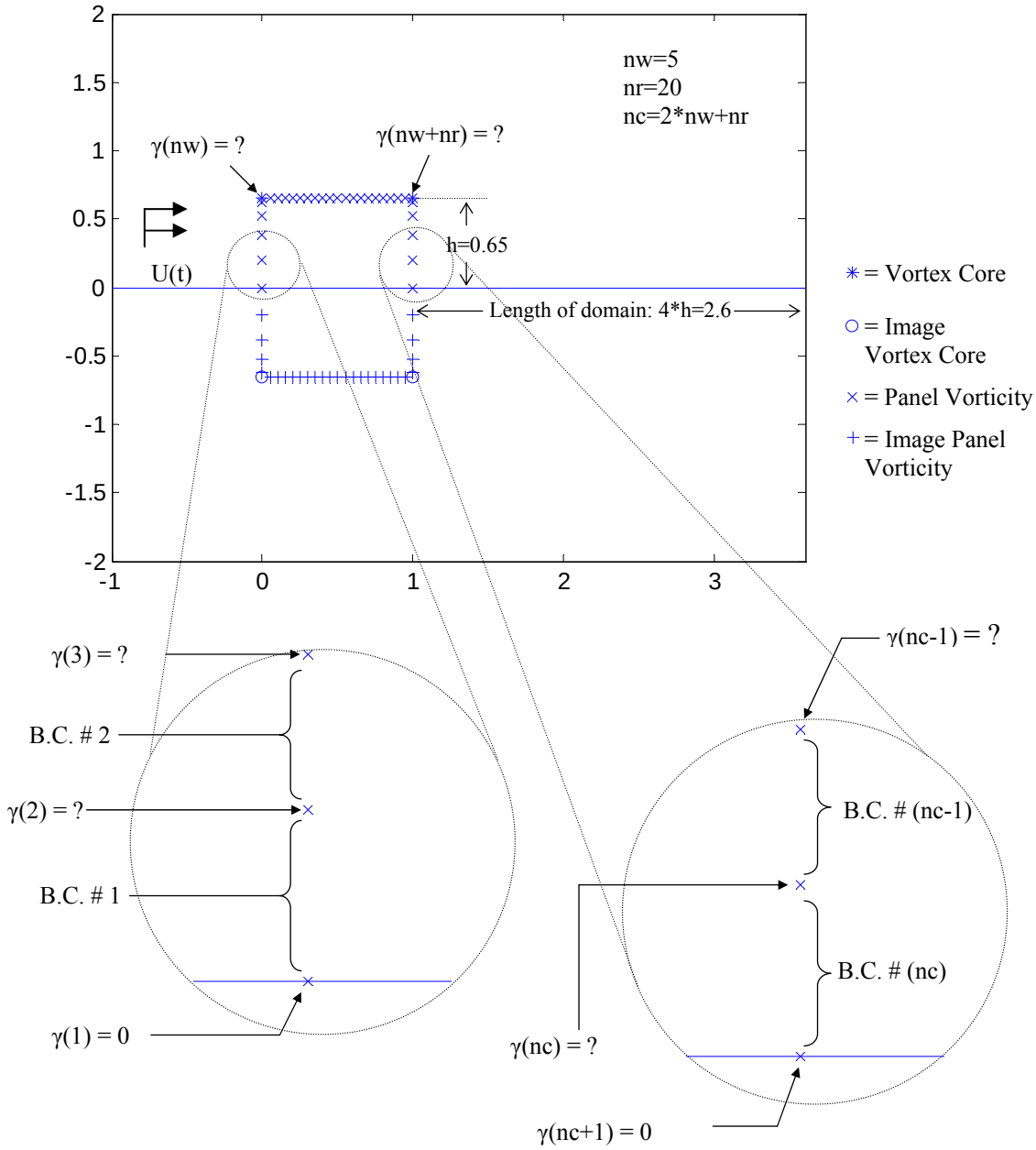

Figure 2.3: Description of Prism Vorticity at time *t=0*

Once the vorticity values associated with each panel and each vortex blob are solved, the two initial vortex blobs are convected to their new location based on the product of the local velocity vector and the time step, Δt. This procedure is then repeated for the duration of the calculation time. If the time step is of interest for calculating the pressure distributions, then an output file containing the values of vorticity for each panel and each vortex blob, as well as the x and y locations of the vortex blobs is created. The

convecting vortex blobs are retained in the computational domain for a length of four times the height of the prism, once reaching this distance the blobs are merely dropped from the flow calculations. A flow chart summarizing the procedure for the main program is presented as Figure 2.4.

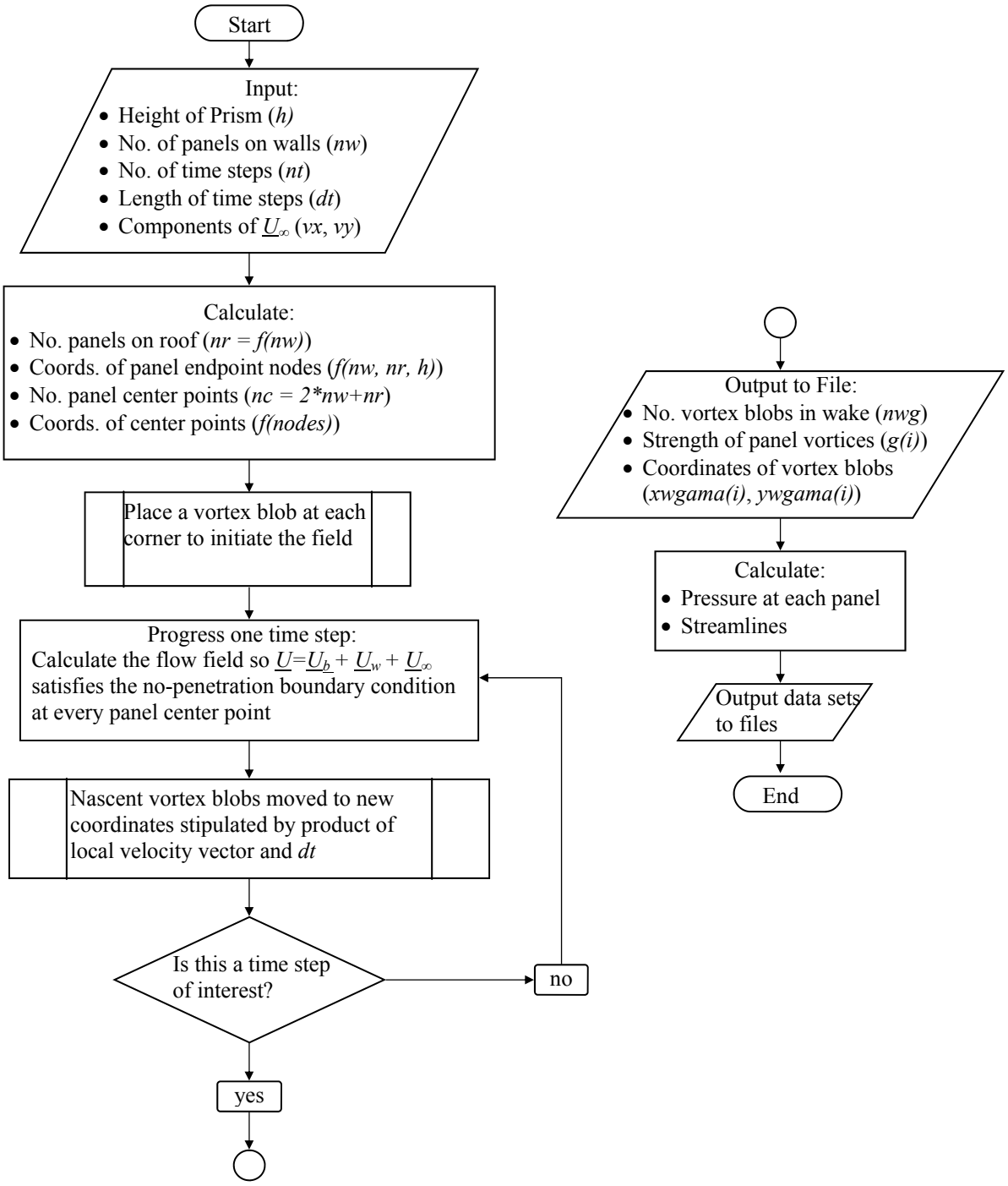

Figure 2.4: Flow Chart Summarizing
Surface-Mounted Prism Routine

2.2.2 Calculation of the Pressure Distribution

The output files from the main program that contain the vorticity calculation is used to create plots of the vorticity field, the velocity field, or the pressure distribution over the surface of the rectangle. Specifically, the pressure distribution is calculated by integrating The Euler equation, written as

$$\frac{\partial u_i}{\partial t} + u_j \frac{\partial u_i}{\partial x_j} = -\frac{1}{\rho}\frac{\partial p}{\partial x_i} \tag{2.2.2}$$

The integrated form of the Euler Equation gives the difference between the stagnation pressure, *p(0)*, and the pressure at a point located a length *l*, measured clockwise along the surface of the rectangle from the origin.

$$p(l) - p(0) = -\rho\left[\frac{d}{dt}\int_0^l \gamma \cdot dl + \frac{\gamma(l)^2 - \gamma(0)^2}{2}\right] \tag{2.2.3}$$

By dividing both sides of Equation 2.2.3 by $\frac{1}{2}\rho V^2$, the pressure coefficient, C_P, at l is given by

$$C_P(l) = 1 - 2 \cdot \left[\frac{d}{dt}\int_0^l \gamma \cdot dl\right] + \gamma(0)^2 - \gamma(l)^2 \tag{2.2.4}$$

where the non-dimensionalized free-stream velocity of 1 is used.

Due to the singularity of the Biot-Savart law, velocity values at the two corners of the rectangle spike, which causes the pressure to approach negative infinity. To alleviate this problem, the γ values in the vicinity of the corners are not used to calculate the pressure. The last acceptable value of pressure on the windward wall before the corner is instead

taken as the left-most value on the roof. Similarly, the right-most acceptable value of pressure from the roof is used as the value for the top of the right wall.

The original code was validated for the case of a rectangular surface-mounted prism with a constant free stream velocity (Qin, et al. 2001). In the next two chapters, the DVM is implemented for two specific applications. In Chapter 3, the original geometry used by Qin, et al. is further explored and improved pressure distributions are found, with some areas for future development. In Chapter 4, the program is slightly varied to calculate the moment coefficient on a bridge cross-section with leading and trailing edge control surfaces. The objective is to implement passive control of the bridge motion using a quasi-steady approach in which the flaps are moved based on the incident flow angle of attack.

Chapter 3

Validating the DVM Code for Wind Loads on Surface-Mounted Prisms

For the DVM code to work properly, correct combinations of parameters must be used: as the number of panels on the surface increases, the length of each time step, Δt, must be decreased. This relationship holds in order to assure that the length, time, and velocity scales associated with the discretisation are all of the same order of magnitude. It is the goal of this chapter to determine how accurate the results generated by the DVM code are for wind over a surface-mounted prism.

3.1 Verification based on Vortex Blob Propagation

Each time step, a vortex blob is introduced into the flow field at the two corners of the prism. As the calculation progresses through time, the coordinates of the vortex blobs can then be used to check the behavior of the velocity field near the prism. If the correct parameters are not selected, discontinuous or otherwise random behavior will be evidenced by unexpected vortex locations. Figure 3.1 shows the building system after the two vortex blobs are placed at the corners and just prior to incrementing the system for the second time step. The full view reveals the relative magnitude of the displacements associated with the first time step, which are approximately 0.005 times the length of the building. The two close views indicate that a small, positive y-component of velocity is present at the leading corner, and an equally small negative y-component develops at the trailing corner. This accurately reflects the dynamics of the flow over a full scale building. The flow "sticks" to the leading edge, resulting in a wrapping effect over the first corner. Similar wrapping behavior occurs on the trailing

corner; here, however, the free-stream velocity draws the vortex farther from the surface of the building than the vertical component does on the leading edge.

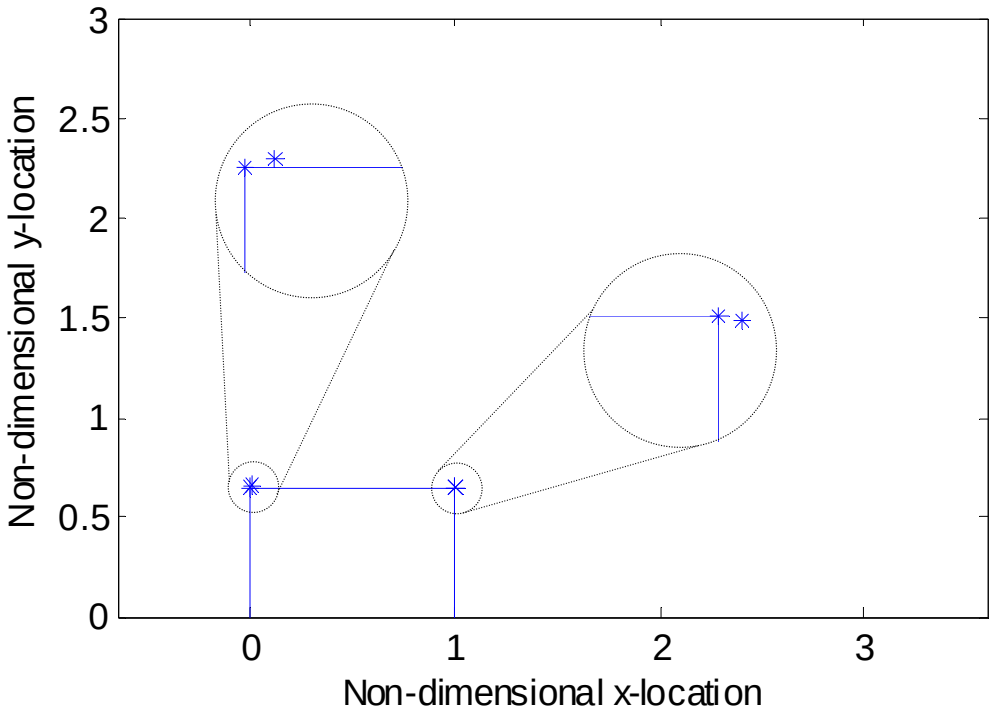

Figure 3.1: Surface-Mounted Prism
System after One Time Step

As time progresses, it is expected that the vortex cores will begin to develop "roll-up" behavior. This rolling of vortices simulates the continuous boundary layer separation inherent to sharp corners. Figure 3.2 shows the progression of the vortex cores through the first 19 time steps. For illustrative purposes, the two corners are shown zoomed to the same scale as the close views of Figure 3.1. It can be seen that after five time steps the vortices begin to propagate back toward the surface of the prism, indicating the initiation of vortex roll-up.

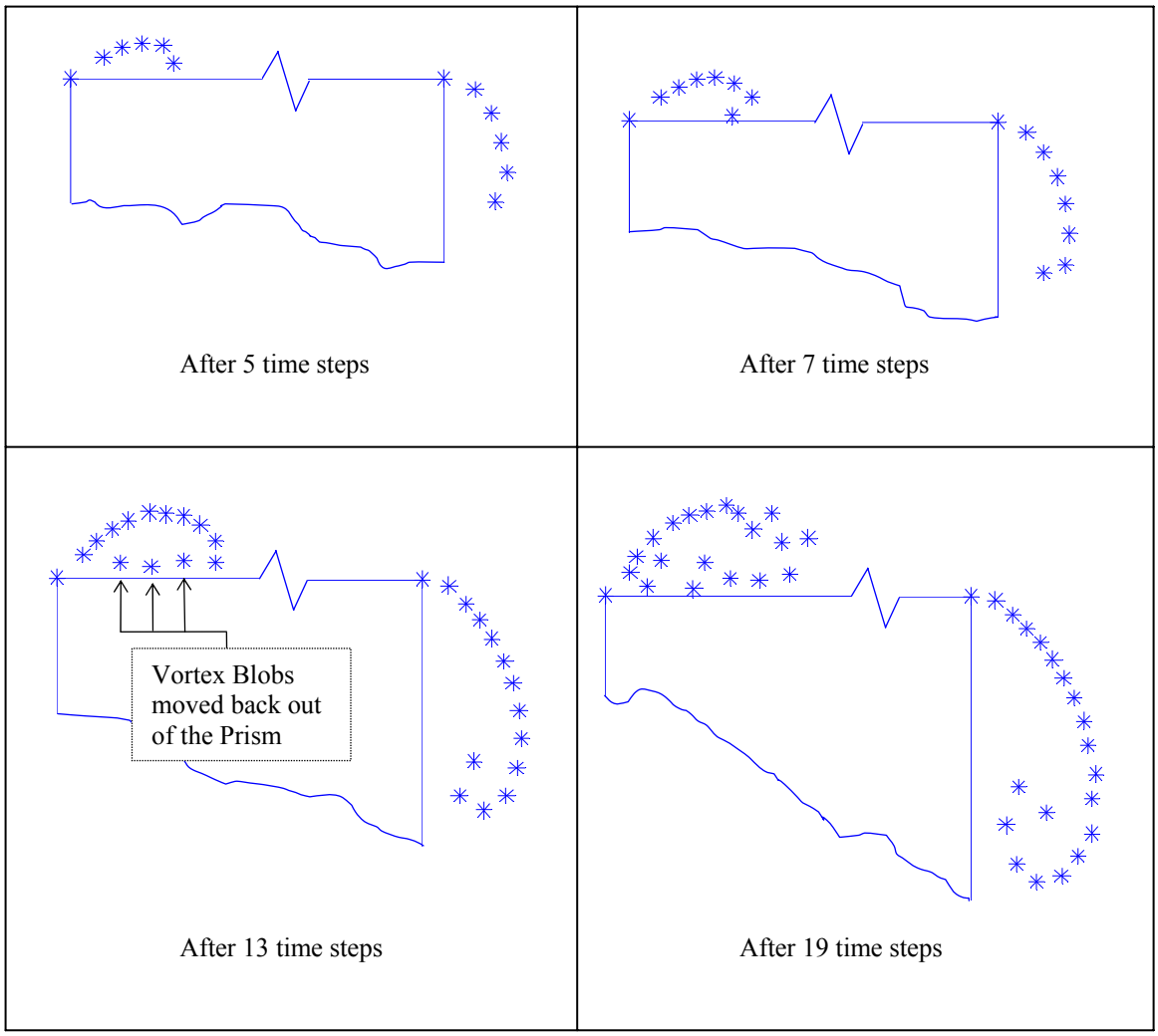

Figure 3.2: Surface-Mounted Prism Vorticity
development through 19 Time Steps

Once the vortex blobs are introduced into the flow field, they are free to convect with the local velocity vector. Consequently, a vortex blob can often develop a velocity vector that moves it within the boundary of the prism. Because the no-penetration boundary condition must be maintained, these blobs are simply moved back across the prism boundary. The evidence of this mechanism can be seen on the leading corner after seven time steps, but more clearly after 13 time steps in Figure 3.2. Instead of a smooth "curl," the lower portion of the structure is awkwardly compressed by the roof of the prism. By the beginning of the twentieth time step, a significant clump of vortices has developed

behind the leading edge corner, indicating accurate development of the separation bubble. The rolling mechanism associated with the coherent vortex structure behind the trailing corner is also clearly present at this time.

After 6,000 time steps, which is equivalent to six dimensionless time units, the flow field has had sufficient time to become fully developed. Figure 3.3 shows the locations of the vortex blobs in the wake at this time. The size of the marker indicating a vortex core is the same as that in Figures 3.1 and 3.2; consequently, the solid region indicates a high vorticity density. Three stream lines are also depicted in Figure 3.3; the locations of the vortex cores fall well in line with the expected stream line configuration. The region of stationary or otherwise slow moving flow, located behind the prism and below the primary streamlines, is indicated. The end of the computational domain, located four prism heights downstream from the end of the prism, where the wake appears to end abruptly, is also labeled in Figure 3.3. When vortex blobs propagate further downstream than this location, they are removed from the flow field, hence the lack of vortex cores beyond this point.

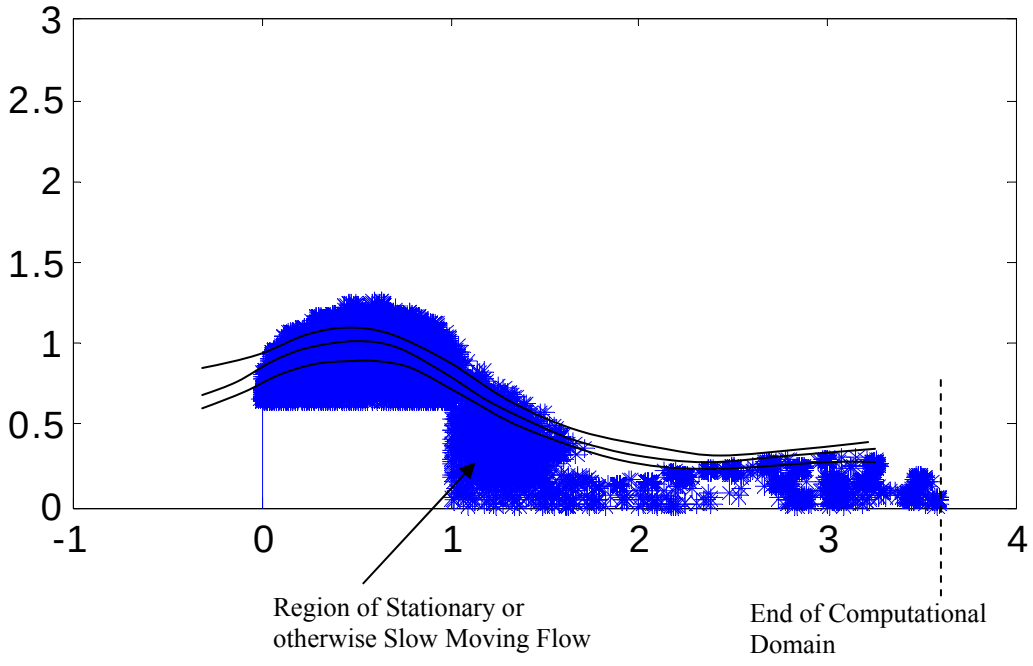

Figure 3.3: Surface-Mounted Prism Vorticity development through 6,000 Time Steps

The vortex propagation behavior, as described by Figures 3.1 through 3.3, indicate the DVM code works to a satisfactory degree. This section reveals that the ratio between the duration of each time step and the length of the vorticity panels has been chosen correctly in order to resolve the vorticity field. Though the Biot-Savart Law, this also means the velocity field is correct for a given time step.

3.2 Verification based on the Surface Pressure Distribution

As described in Chapter 2, a non-dimensional free-stream velocity of one is used to progress the vorticity field during each time-step. The free-stream velocity is implemented over the entire domain instantaneously during the first time-step; therefore, any behavior associated with a developing flow is due solely to the vorticity field. Until the vortex blobs shed from the windward corner have progressed far enough down stream to interact with the vortices shed from the leeward corner, the flow is considered not fully-developed.

In order to assure the developing portion of the flow simulation is surpassed, the first 6.5 time units (6,500 time steps) are not used to calculate the surface-pressure distribution. After 3.6 time units a theoretical vortex blob progressing at the free-stream velocity of one will propagate 3.6 prism lengths, enough to travel from the windward corner of the building downstream and out of the computational domain.

The change in surface vorticity over an incremental length of time can be used to calculate the pressure distribution on the surface of the prism. For the analysis presented here, the pressure was calculated over an interval of one time step at the beginning of every one hundred. This technique produces ten pressure calculations per time unit; averaging several of these over a length of time gives a better description than any one.

To produce expected pressure distributions, the duration over which the average is taken becomes paramount.

Figure 3.4 shows both the mean value and the standard deviation of the pressure coefficient, C_P, at each node from the 6,500th to the 10,000th time step. The mean, therefore, represents an average of 35 time series. The locations of the two corners are indicated by the two vertical, dashed lines.

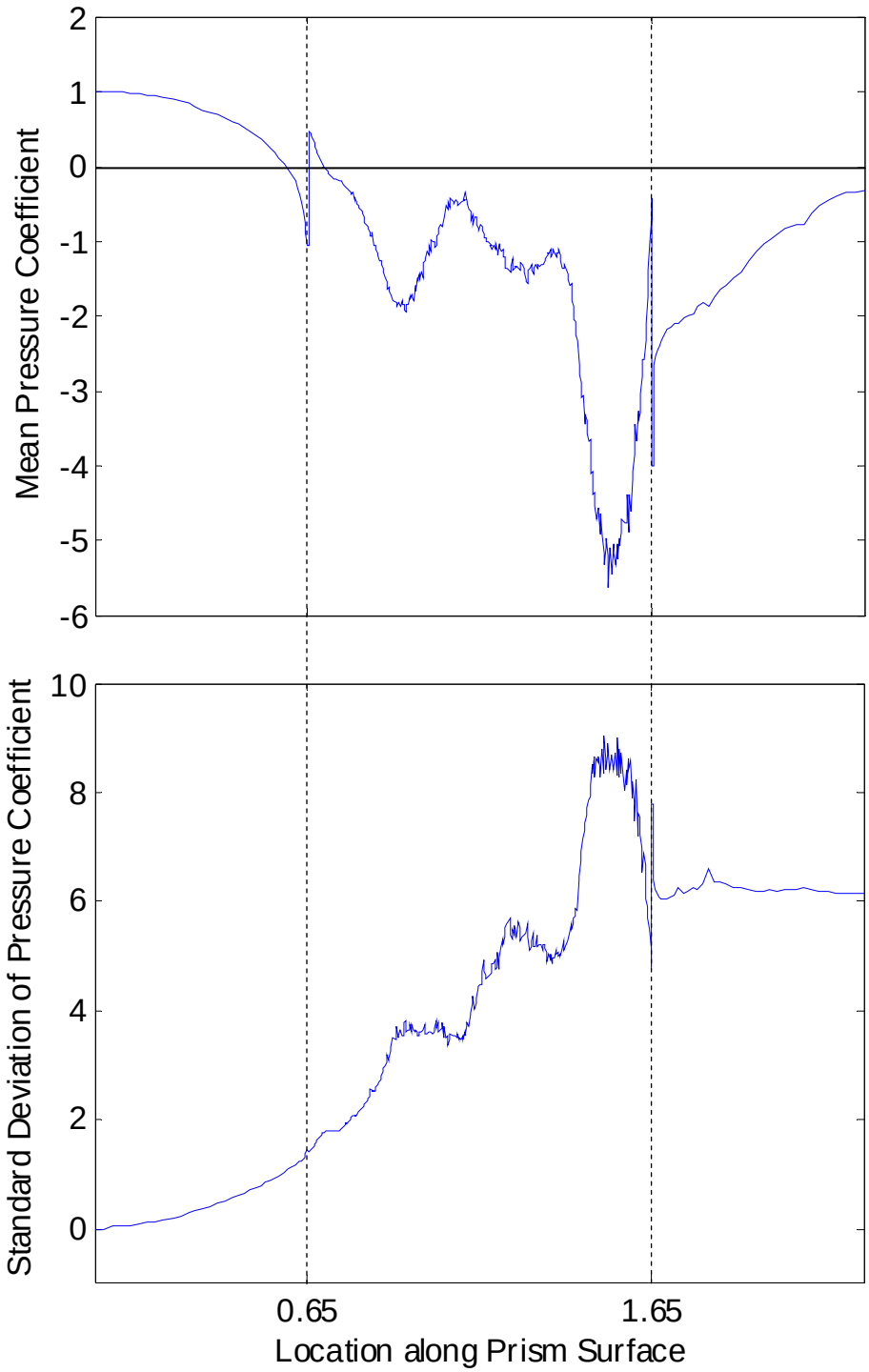

Figure 3.4: Mean and Standard Deviation between 6,500th and 10,000th Time Step

The standard deviation, indicating the variability of the data, increases over the front face and the roof. Generally speaking, the standard deviation is expected to remain small over the whole surface. The high magnitude values obtained for the standard deviation indicate that at least one of the following is true: fully-developed flow is not reached, even after 6,500 time steps; the mean should be calculated over a longer duration; or more pressure distributions should be calculated for each time unit.

Figure 3.5 shows a comparison between the mean pressure distribution from above and results generated by Elsayed, et al. (2005) for a similar surface-mounted prism. The height of the prism used by Elsayed, et al. however, is slightly smaller than that of the prism implemented with the present code. To match the scales, the three portions of the plot representing the three different surfaces have been resized in order for the locations of the corners to line up vertically. This can be seen in Figure 3.5; the scale on the dependent axis has also been inverted to follow the convention used by Elsayed, et al (2005).

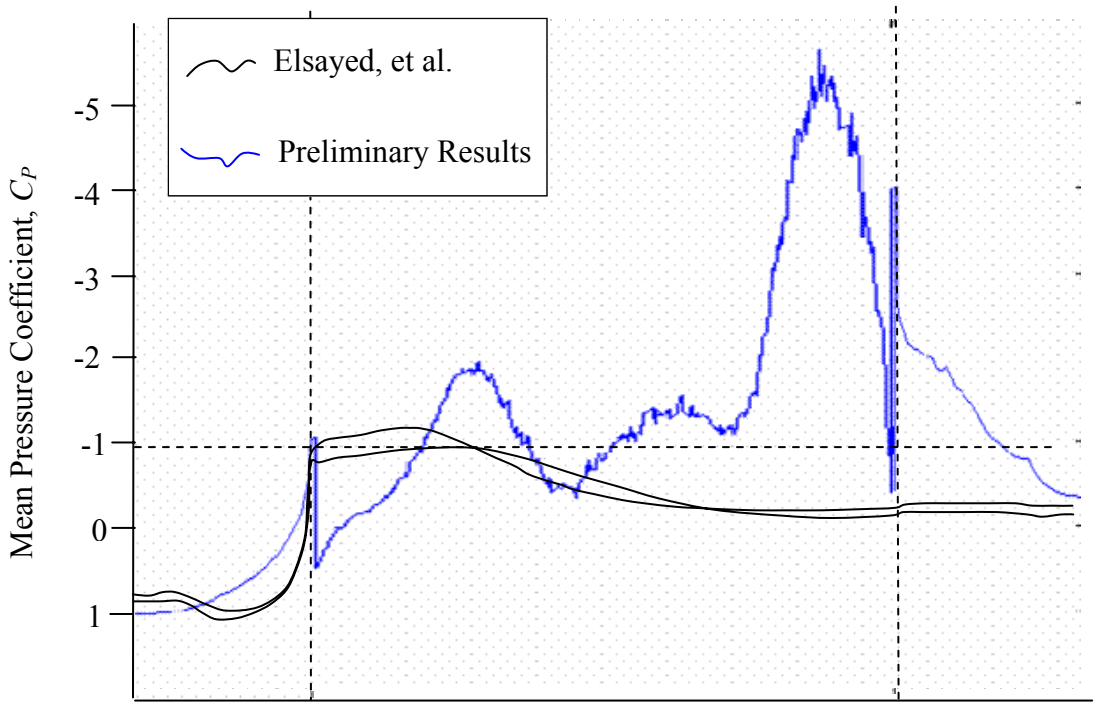

Figure 3.5: Comparison of Mean C_P with Results from Elsayed, et al. (2005)

It can be seen that the results for the two walls match well with those of Elsayed, et al. On the leading edge, the pressure decreases from 1 at the ground to approximately -1 at the corner. Negative C_P are also found on the leeward wall; the value at the ground is less than -0.5, which is what Elsayed, et al. and Hwang, et al. (1999) found as well. It should be noted that the values calculated on the leeward wall represent a significant improvement over the results originally obtained by Qin, et al. (2001). Finding only positive values for this region, the parameter values chosen by Qin, et al. are not optimal for the particular prism configuration.

3.3 Conclusions and Future Work

In order to improve the surface-pressure calculations from the DVM code, several possible avenues should be explored. Given the accuracy of the vortex core propagation and the magnitude of the pressure's standard deviation, it is thought that a better solution can be found by averaging over more pressure calculations. This can be accomplished in two ways: increasing either the sampling frequency or the sampling time. The current sampling frequency is one value every 100 time steps, which gives ten data sets for each non-dimensional time unit.

It is expected that a more accurate mean value would be found by calculating over a longer time period. A dimensionless sampling time can be generated from the actual sampling time, T, using the height of the prism, h, and the free-stream velocity, U_∞. For the DVM results, Equation 3.3.1 gives this calculation.

$$\frac{U_\infty T}{h} = \frac{(1)(3.5)}{0.65} = 5.38 \qquad (3.3.1)$$

Building codes require that wind measurements in full scale be taken for at least 15 minutes to develop accurate estimates of the mean, rms, and peak values of the pressure

coefficients. For a modest wind speed of about 40*m/s* over a building that is about 5*m* high. The required 15 minutes translates to a dimensionless sampling time of

$$\frac{U_\infty T}{h} = \frac{(40\,{}^{m}\!/_{s})(15\,\text{min})(60\,{}^{s}\!/_{\text{min}})}{5m} = 7200 \qquad (3.3.2)$$

Obviously, this is much larger than the dimensionless time used in the calculation presented above. Additionally, the results generated by Qin, et al. (2001), which give good, low standard-deviation results on the roof, are calculated over 132 non-dimensional time steps. Converting this into the dimensionless sampling time, as described above, using the prism height of 0.65 gives a value of 203. Although this is not of the same order of magnitude as the real world case, it is still two orders of magnitude larger than the current calculation time. Based on this order-of-magnitude analysis, the DVM calculation should be allowed to run for a much longer time period.

Using seven parallel processors, the calculation requires approximately 24 hours to increment 2,000 time steps once the flow becomes fully developed. The principle of super-position holds for the velocities calculated from the Biot-Savart Law for every vortex panel and core; consequently, a more extensive cluster of computers would greatly decrease the computational time required to develop an accurate pressure distribution. This represents an avenue to explore in the future for this new CFD technique.

Chapter 4

Aerodynamics of Wind Flow over a Bridge Deck with Flaps

In this chapter, the Discrete Vortex Method is used to develop a quasi-steady approach to determine the effectiveness of a particular air-flow control system for a bridge deck. Two wedge-shaped flaps are placed on the windward and leeward sides of the simulated bridge deck; these can be rotated to affect the net flow pattern. The dependence of the resulting aerodynamic force components, especially the cross-sectional moment, on the angle of attack and the two deflection angles is discussed. Ultimately, a control law is defined for the two flap angles to minimize the aerodynamic moment for a known angle of attack.

4.1 Introduction

Much research has been done to understand the aerodynamic and structural factors of bridge design that cause responsive motion to normal wind loads. Initially, research focused on wind-tunnel tests; economic concerns, however, have necessitated the development of accurate computational routines. Several theoretical air-flow control systems have been proposed in this manner, with varying results.

4.1.1 Background

Kobayashi et al. (1992) were the first to propose a bridge stabilizing system based on air-flow control. Two wings positioned below the bridge deck were oriented so as to generate aerodynamic forces that stabilized the bridge in the lift, drag, and moment senses. Through wind tunnel experiments, this system was found to double the threshold

wind speed at which flutter began. Additionally, equation of motion analysis of the deck-flap system was used to develop a control law for the orientation angel of the flaps (Wilde, et al, 1998). The criteria used by Kobayashi et al. (1992) for their feedback system were the angle and rate of angular displacement of the bridge deck from the undisturbed position; later control system designs would continue this trend.

Wilde et al. (2001) developed a system with the control surfaces attached to the edges of the bridge deck. The Theodorsen function was used to define the orientation of the flaps in the same manner as the control system developed by Kobayashi et al (1992). The flaps were 'pinned' to the center-line of the bridge deck, but the position of the point of rotation was optimized along the length of the flap cross-section. This variable distance from the edge of the bridge deck, δ, is represented in Figure 4.1, which presents a close view of the trailing edge flap and bridge deck; the deck has been deflected to an arbitrary angle, β. It was found that the optimal length for δ was zero; the flaps should be pivoted about the edges of the bridge deck, as shown in Figure 4.2

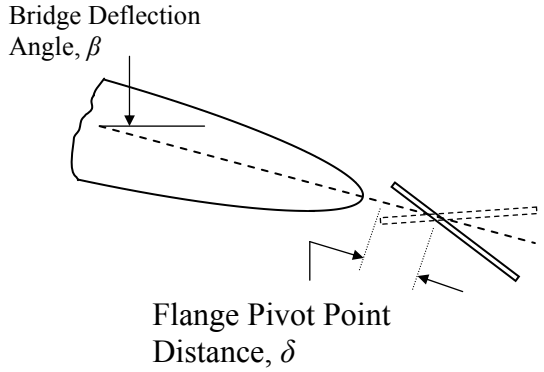

Figure 4.1: Deck-Flap System (Trailing Edge View) for
Arbitrary Flap Pivot Point Distance, δ (Wilde, et al. 2001)

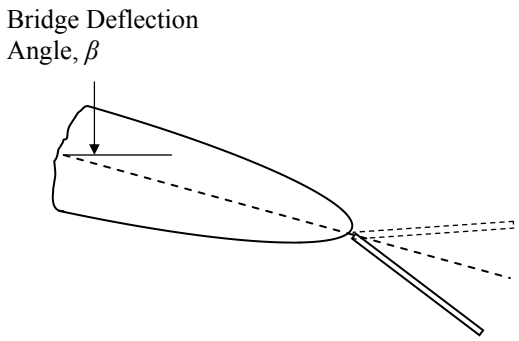

Figure 4.2: Deck-Flap System (Trailing Edge View) for
Optimized Flap Pivot Point Distance, $\delta=0$ (Wilde, et al. 2001)

A bridge-flap system designed by Vezza, et al. (2003) implemented a singular control flap on the leading edge that was two-dimensional in cross-section. All previous flap designs reflected the comparably small aspect ratio wing-like structures originally proposed by Kobayashi et al (1992). Similar to the design presented by Wilde et al. (2001), this triangular flap was pivoted about the edge of the bridge, but the attachment point was moved from the center-line to the lower deck face. Although this allowed the control surfaces to be easily deflected to large angles relative to the bridge deck, rotation of the flaps produced a gap between the upper surface of the deck and flap. A close view of the leading edge flap and bridge deck demonstrating the pivot point of the flap and upper surface gap is shown in Figure 4.3. The Discrete Vortex Method was used to analyze the flow behavior around the bridge deck for various angles of attack and flap deflection angles. It was found that the upper-surface gap produced flow behavior that hampered the effectiveness of the control system. Despite this drawback, it was shown that the two dimensional flap helped delay the onset of flutter conditions for the bridge.

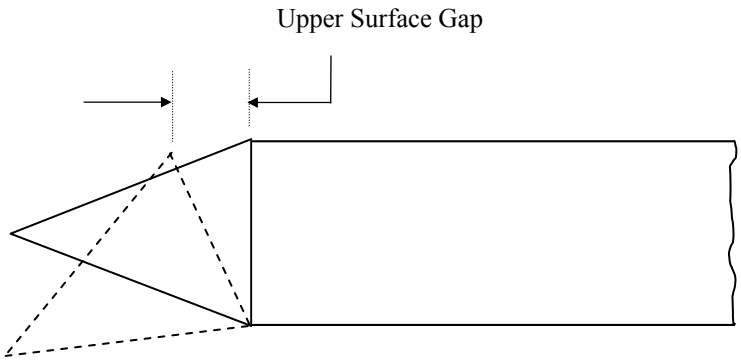

Figure 4.3: Leading edge Deck-Flap System with
Flap Deflected, proposed by Vezza et al (2003).

4.1.2 Proposed Flap Design

The conclusions reached by Vezza et al. (2003) and Wilde et al. (2001) were used to generate the proposed flap design. In keeping with the former, a high aspect ratio design was selected. The edge of the bridge deck was again used as the location of flap rotation; following the results of the latter, however, the pivot point was moved from the bottom bridge face back to the center-line of the deck. In order to eliminate the upper-surface gap that developed in the design of Vezza et al (2003), a circular component was added to the side of the flap directed toward the inner portion of the bridge deck. Consequently, as the flap is deflected, the rounded surface extends beyond the bridge deck, maintaining structural continuity between the flap and the deck. In order to create the necessary geometrical clearances for larger flap deflections, rotating surfaces were added to the upper and lower deck faces. A view of the windward bridge-flap system in the neutral position and deflection to a positively defined angle θ_W, is shown in Figure 4.4. For both the windward and leeward edges, counterclockwise rotations of θ were defined as positive. Also presented in Figure 4.4 is the rounded extension of the deflected flap past the edge of the upper deck surface in addition to the rotated clearance flap of the lower deck surface, which allows the control flap to be retraced into the deck.

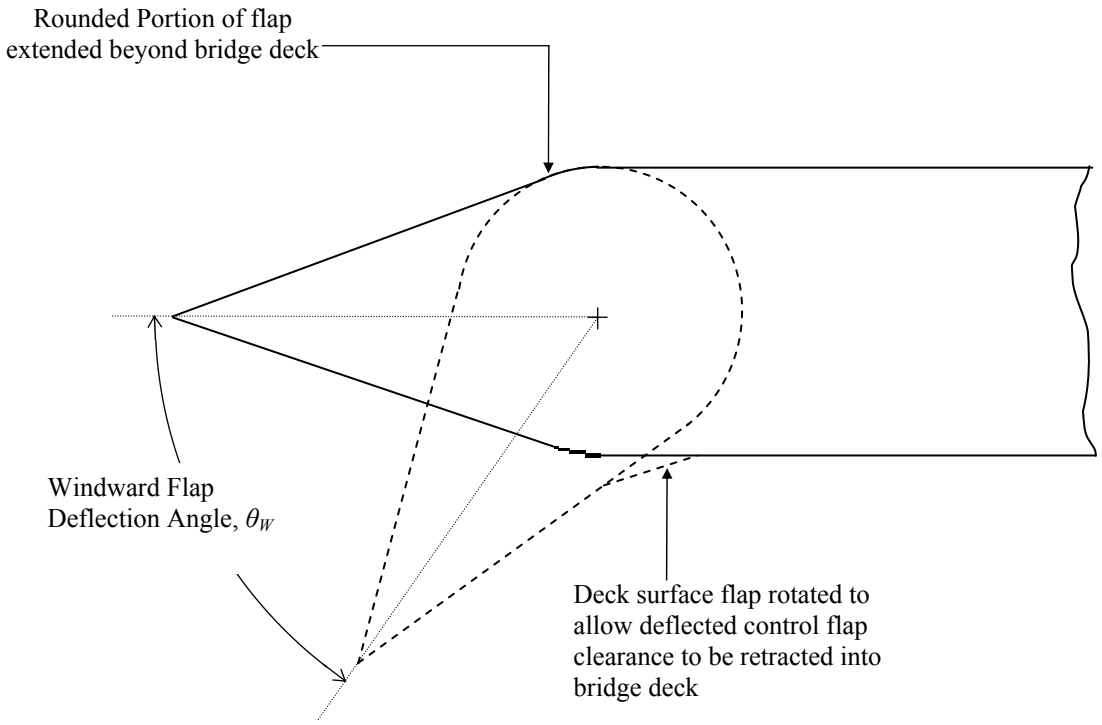

Figure 4.4: Proposed Bridge-Flap Design (Windward Edge View),
Demonstrating Range of Motion and Geometrical Clearances

4.1.3 Experimental Methodology and Objectives

The calculations presented in this work establish the framework for a method to passively control the motion of a bridge. The quasi-steady approach is used to minimize C_M for a given angle of attack by moving both the leeward and the windward flaps. The optimal configurations defined as such can then be implemented for an approaching incident wind with a known angle of attack.

Five vales of the front and rear flap deflection angles, θ_W and θ_L, are used to develop the initial set of C_M values. All possible combinations of -25º, -12.5º, 0º, 12.5º, and 25º give a total of 25 different configurations of the dual flap-bridge system with which the effect of each flap can be determined independent from one another. For deflection angles much larger than 25º stall behavior becomes a concern, which would reduce the effectiveness of the aerodynamic system. The case presented in Figure 4.5 shows θ_W = 12.5º and θ_L = 25º. Figure 4.5 shows the five possible configurations of the front and rear flaps. For the cases where either θ value has a magnitude of 25º, the tip of the flap can be seen to lie outside the vertical range defined by the width of the deck.

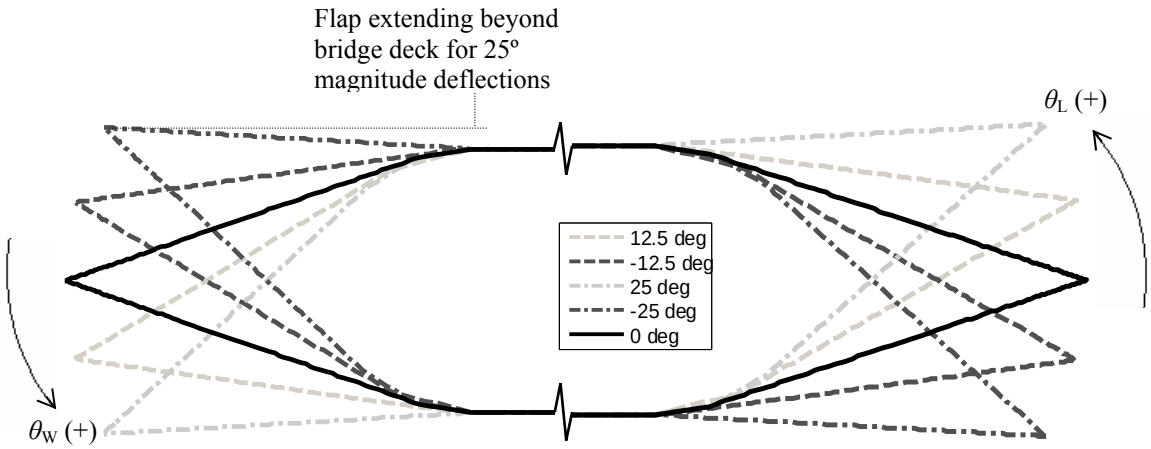

Figure 4.5: Orientations of Flap Deflection
Angles Used to Develop the Control Law

The primary mode of bridge motion that leads both to structural failure and pedestrian discomfort is the torsional mode (Wright, 2004). By minimizing the cross-sectional moment coefficient, C_M, the twisting behavior inherent to this form of harmonic behavior can be avoided. Consequently, analysis focuses on the ways in which this quantity varies with the different flap configurations. Configurations that would lead to zero moment values are extrapolated from plots of C_M versus θ. Several proposed configurations of θ_W and θ_L are validated using the DVM code to check the moment coefficients that develop.

For each angle of attack, $\alpha=0$º, 5º, and 10º, a control relationship is defined via a contour line which minimizes the moment coefficient.

4.2 Computational Approach

The magnitude Reynolds numbers associated with wind flow over a bridge are on the same order as those encountered with the building approximation. Therefore, the inviscid approximation again applies in this case. The computational approach is primarily the same for the bridge deck application as the low-rise building; some modifications were made, however, reflecting the different goals of this section. The purpose of the control system is to affect the net behavior of the whole cross-section; consequently, the way in which the effect of the flow varies over the cross-section is not important. The vorticity field is therefore used not to analyze the surface pressure distribution, but the moment coefficient for the entire section.

4.2.1 Implementation of the Discrete Vortex Method

In similar fashion to the low-rise building, the geometry of the deck-flap system was greatly simplified before the surface could be discretized. A rectangle with an aspect ratio of 8.75 was used to simulate the deck; normalized to the thickness of the deck, the two flaps have a length of 1.374. To define a specific geometrical configuration using the same length-scale as that associated with the surface-mounted prism, a deck thickness of 0.4 was used. This reduced the deck width, b, to 3.5, and the length of each flap, a, to 0.5495. The angle between the two sides of the flap, φ, as constrained by the specific geometry selected, is 42.7º; these relationships can be seen in Figure 4.6.

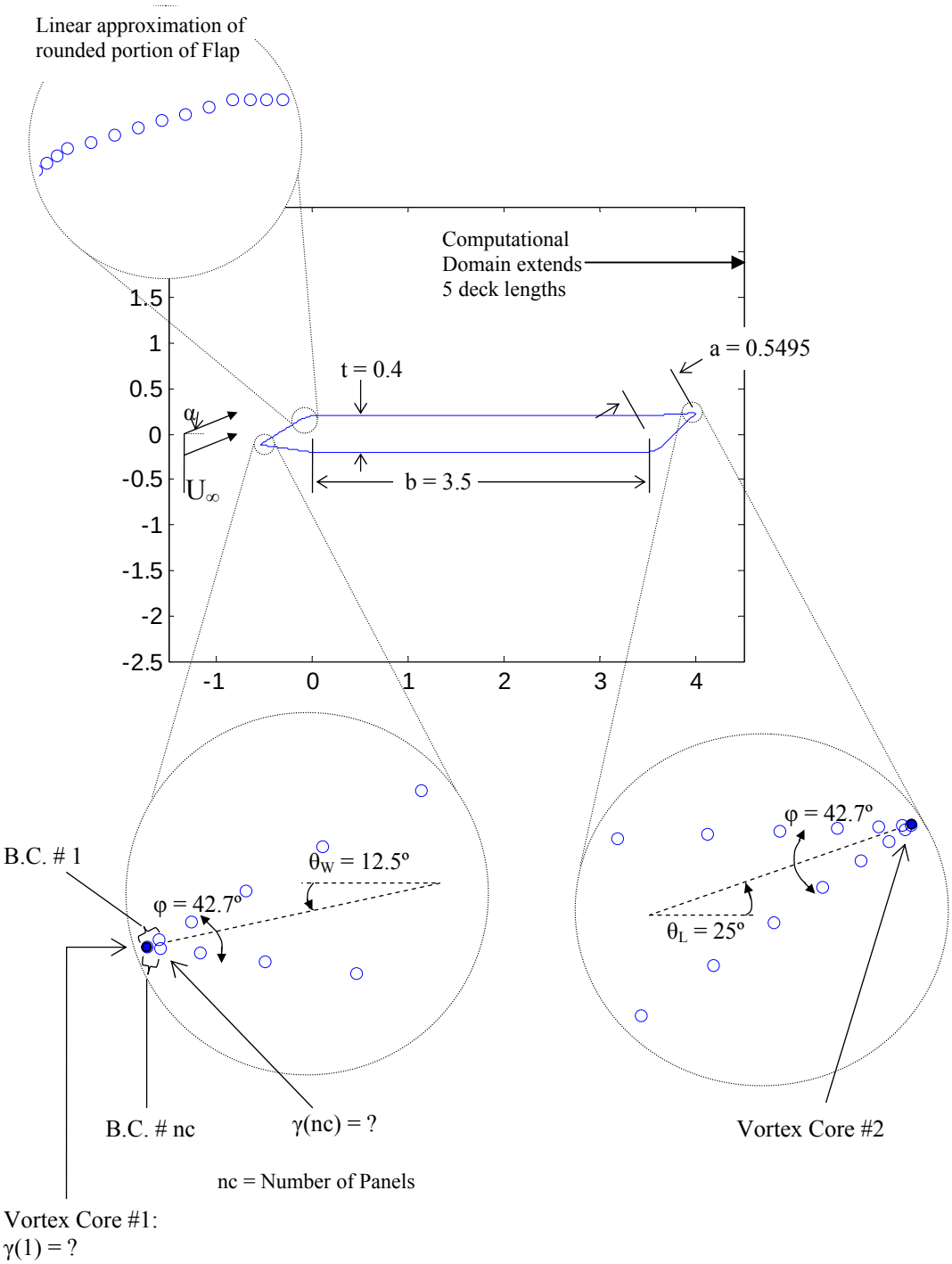

Figure 4.6: Description of Bridge Cross-Section Vorticity at time *t=0*

To remove the effects associated with mounting the prism on a surface, mirror image vortices were no longer used; in stead, surface vorticity was distributed on the bottom of

the bridge, as seen in Figure 4.6. More consideration must be made to the separation behavior of the bridge cross-section, than the prism. Clearly, separation occurs from the ends of the two flaps; what is not as obvious is the flow behavior in the region where the flaps meet the bridge deck. For small angles of attack, the flow will not separate so long as the linear approximations of the rounded portion of the flaps do not develop significantly sharp corners. Given this vorticity shedding scheme, a vortex blob is convected into the flow field solely from the ends of both flaps during each time step.

Figure 4.6 represents the initial configuration of the system; the two vortex cores are located at the ends of both flaps, taking the place of the panel vorticity at these points. Similar to the walls of the building, a sinusoidal distribution of nodes is used on the upper and lower surfaces of the flaps in order to solve for a continuous flow field while maintaining an optimal computational time.

Because the geometry used in this application creates a closed loop of vortex panels, unlike the prism problem, the number of unknown γ values is the same as the number of panels. This can be seen in the zoomed view of the leading edge presented in Figure 4.6. Because of this redundancy, within the computational routine the no-penetration boundary condition given by one panel must be eliminated in order for the coefficient matrix to be non-singular.

The structure of the DVM code is similar for this application, although a few changes are important to note. 100 panels with a sinusoidal distribution are used on the two faces of the flaps; a linear distribution that gives a comparable panel length is used on all other faces. To coincide with the number of panels, the time step was set to 0.006. Critical values of the deflection angles occur at positive and negative 20º. When the flaps reach these angles, the "deck surface flap" as described in Figure 4.6 must be rotated to allow enough clearance for the flap to be retraced into the bridge deck. Although 25º is the largest magnitude flap deflection analyzed, the program allows for rotations of up to 75º. The three ranges of θ that are relevant to the computer code can be seen in the flow chart presented as Figure 4.7.

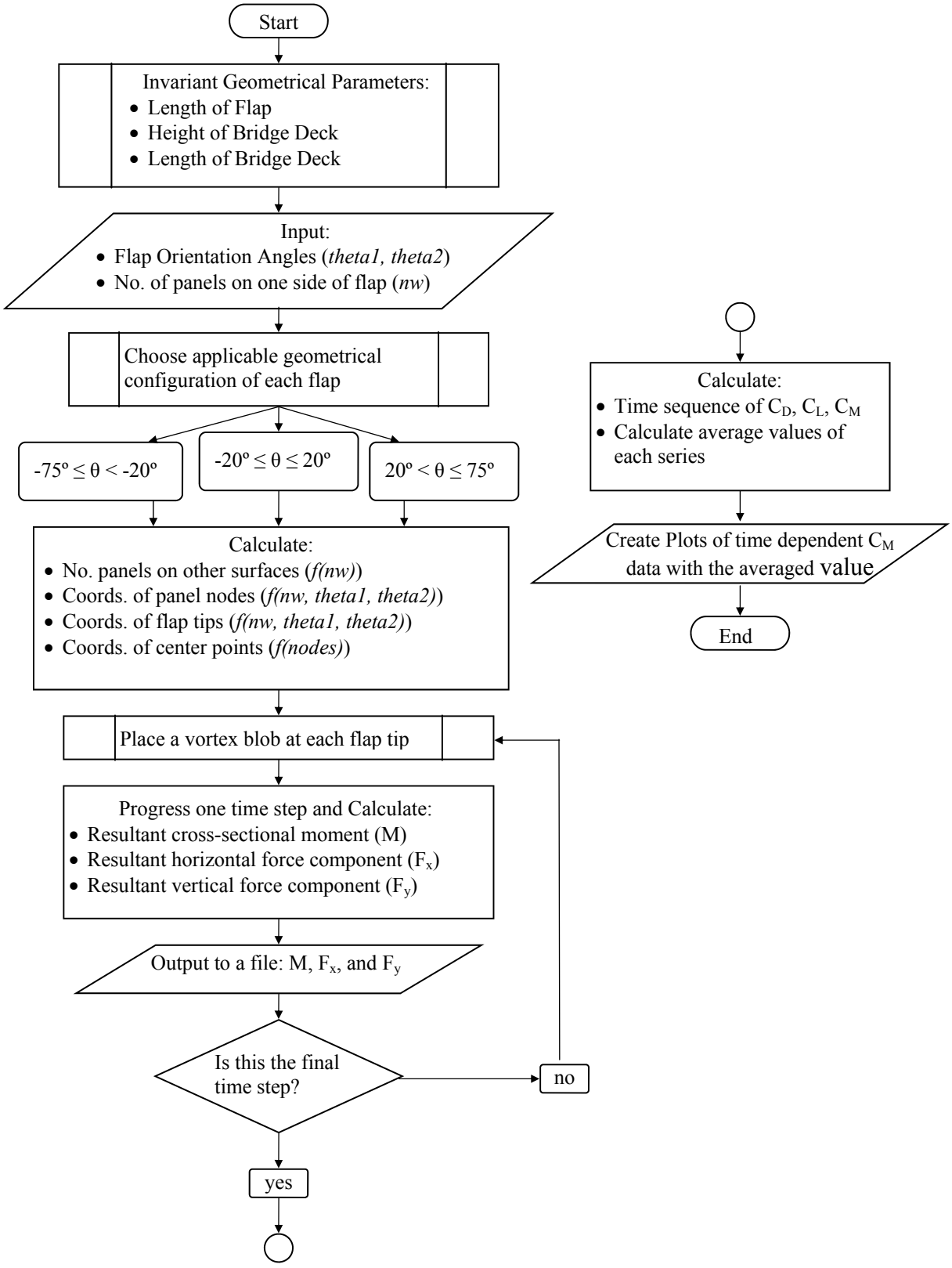

Figure 4.7: Flow Chart Summarizing Bridge Cross-Section Routine

4.2.2 Calculation of the Moment Coefficient

For each time step, as described in Figure 4.7, the program calculates two resultant force components from the pressure distribution as well as the resultant moment these forces generate about the bridge cross-section. By applying a process similar as that described in Section 2.2.3, the pressure distribution is found over the cross-section. Because pressure, in this case, is defined as a force per unit length, the pressure value at each node is multiplied by the length of the element to give a force vector normal to the surface of the body. These force vectors are then broken into their horizontal and vertical components. The case shown in Figure 4.8 has the i^{th} pressure force broken into its x-component, F_{xi}, and y-component, F_{yi}. As described by the moment equation in the figure, where counterclockwise moments are considered positive, the coordinates of the panel center points can then be used to calculate the moment each force component generates about the origin. The total cross-sectional moment is then found by summing these values.

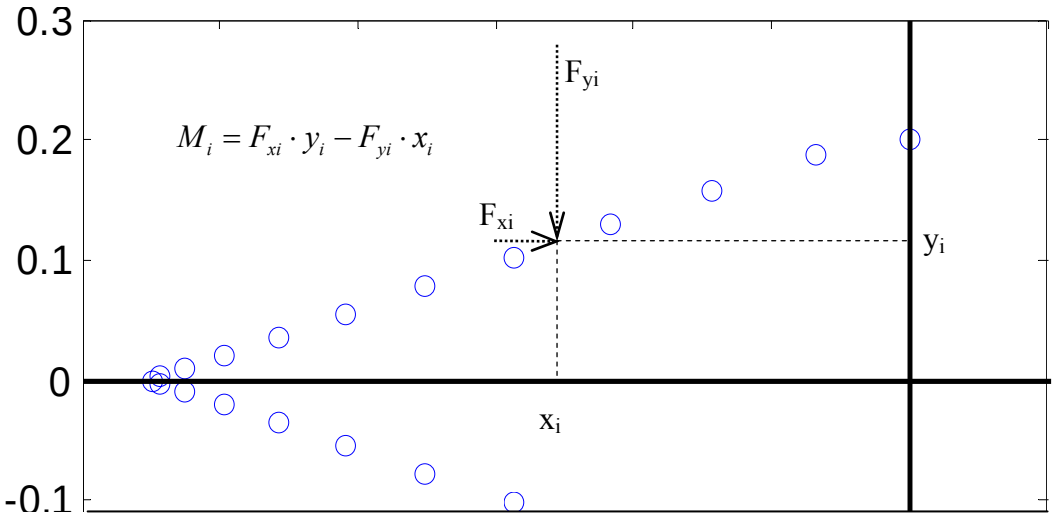

Figure 4.8: Calculation of the Moment due to Resultant Pressure Force acting on a Panel

Using the overall non-dimensional length of the cross-section, 4.7, the aerodynamic moments are normalized by Equation 4.2.1 to generate dimensionless moment coefficients for a unit depth, b. The "moment" calculated by the program has an inherent density factor, ρ, which cancels from the numerator when the dynamic pressure is introduced into the denominator, as shown in Equation 4.2.1.

$$C_M = \frac{Moment}{\frac{1}{2}\rho U_\infty^2 l^2} = \frac{2 * Moment}{(4.6)^2} \tag{4.2.1}$$

Because each discrete vortex calculation begins with no vorticity in the flow field, the first portion of the data represents a significant transient phase as the wake develops. To meet the quasi-steady criteria, the first 5000 data points (representing 30 non-dimensional time units) are eliminated before calculating the running average and the mean value of the moment data. An additional problem develops as each vortex core reaches the end of the computational domain and is subsequently removed; a spike results in the data series. Values surpassing more than one standard deviation from the mean are considered points of singularity and are removed from the data set. The mean is then recalculated using this more reliable data set.

4.3 Results and Discussion

In order to determine the dependence of the cross-sectional moment coefficient on each of the flap deflection angles independently, four series of plots were generated. For the three angles of attack, by holding the windward angle constant, C_M is plotted versus the leeward angle, θ_L. Conversely, a set of plots are created by holding the leeward angle constant and plotting C_M versus θ_W. Additionally, while holding θ_W constant, C_M is plotted versus the angle of attack, α, for each value of the leeward angle.

Figure 4.9 presents plots of C_M v. θ_L for three constant values of θ_W (-12.5º, 0º, and 12.5º). The geometry of the windward angle that is associated with each plot is shown for clarity. Callout boxes are used to identify and describe values of the leeward angle for which the mean moment coefficient is zero, indicating a possible control law configuration for the particular angle of attack. For Plot A of Figure 4.9, the 10º angle of attack data changes sign (indicating a zero) for an approximate θ_L value of 5º. Similarly, the data for $\alpha=5^o$ gives a zero value for one of the tested configurations, $\theta_L=0^o$ and $\theta_W = -12.5^o$. Plot B reveals a possible zero C_M configuration for each angle of attack. As expected, for $\alpha=\theta_L=\theta_W=0^o$ vertical and horizontal symmetry is achieved in the flow field, leading to a zero value of the moment coefficient. The data for $\alpha=10^o$ reveals a trend through which another zero point can be extrapolated. Plot C, where $\theta_W=12.5^o$, three more zero moment values are found; however, the value obtained by extrapolating from the 10º angle of attack data leads to a leeward angle deflection large enough to where stall becomes a concern.

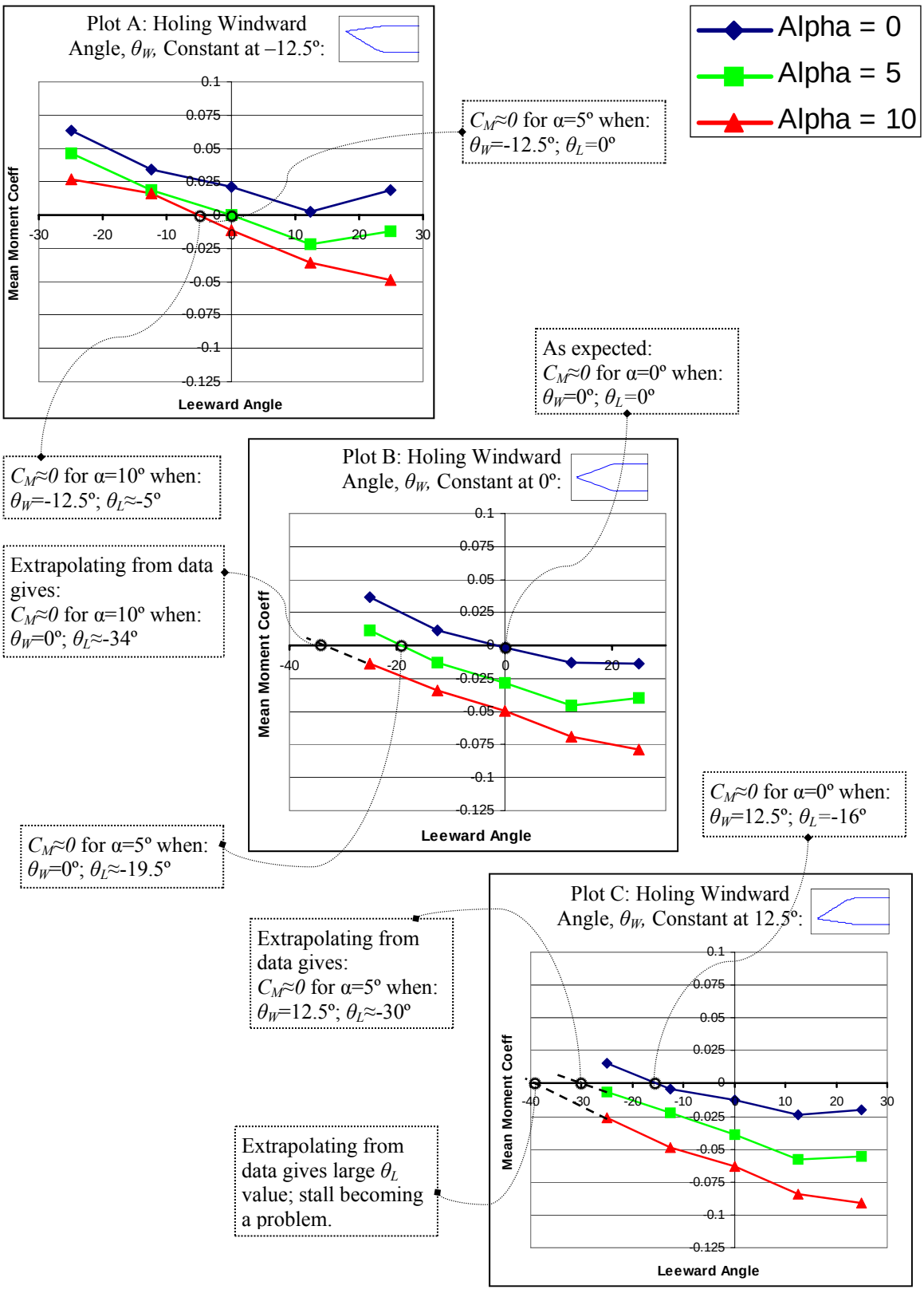

Figure 4.9: Three Plots of C_M v. θ_L for each α holding θ_W constant

Two more plots, following the pattern of the ones presented in Figure 4.9 were generated for the configurations where θ_W=*-25°* and θ_W=*25°*; these exhibit similar trends. Table 4.1 summarizes the feasible configurations which lead to zero moment coefficient values for the five tested orientations of the windward flap.

Table 4.1: Feasible Configurations for Control Flaps for the tested θ_W values

Angle of Attack, α	Windward Flap Deflection Angle, θ_W	Leeward Flap Deflection Angle, θ_L
0	0	0
0	12.5	-16
5	-25	10
5	-12.5	0
5	0	-19
5	12.5	-30
10	-12.5	-5
10	0	-34

By holding the leeward angle, θ_L, constant, the dependence of the moment coefficient on the windward angle can be found. Three similar plots to those of Figure 4.9 are presented in Figure 4.10 that show this behavior. As evidenced in Figure 4.9, increasing the windward angle (ie. moving from Plot A through B to C) causes a downward shift in the three angle of attack data sets. This trend surfaces in Figure 4.10 as a generally negative slope for the data of Plots A, B, and C. The inverse relationship holds: the negative slope exhibited in Figure 4.9 leads to the downward shift in data from Plot A to Plot C of Figure 4.10.

In similar fashion to Figure 4.9, configurations of the two flap angles which result in a zero C_M value are identified by callout boxes. For Plot A, where the leeward angle is held constant at -12.5º, four changes in sign occur in the data; however, only three points are reliable. The drastic change in trend of the $\alpha=10^o$ data after θ_W=-12.5 indicates that the data point for $\theta_W=-25^o$ and $\theta_L=-12.5^o$ represents a change in the flow characteristics.

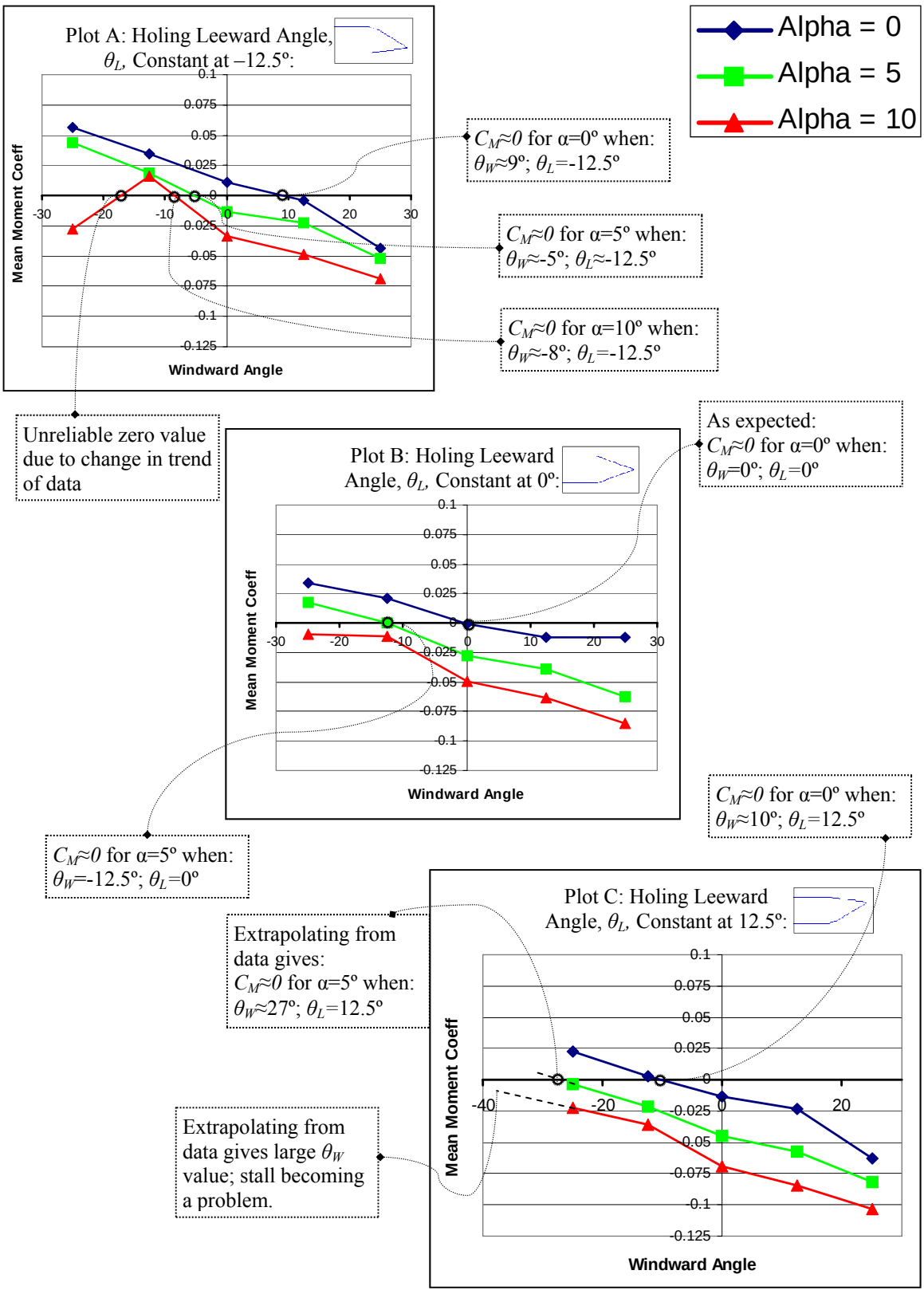

Figure 4.10: Three Plots of C_M v. θ_W for each α holding θ_L constant

A summary of the feasible configurations leading to a zero moment coefficient value using the five tested leeward angle values is shown in Table 4.2.

Table 4.2: Feasible Configurations for Control Flaps for the tested θ_W values

Angle of Attack, α	Windward Flap Deflection Angle, θ_W	Leeward Flap Deflection Angle, θ_L
0	20	-25
0	9	-12.5
0	0	0
0	10	12.5
0	-5	25
5	8	-25
5	-5	-12.5
5	-12.5	0
5	-27	12.5
10	-4	-25
10	-8	-12.5

A process similar as that presented in Figures 4.9 and 4.10 is used to deduce for which angles of attack the 25 analyzed configurations would yield zero moment coefficient. This is accomplished by plotting the moment coefficient verses the angle of attack for each leeward angle while holding the windward angle constant. Due to the symmetry of the system, negative angles of attack have no relevance; therefore, no data was extrapolated into this range. Figure 4.11 presents two plots to demonstrate some of the predicted angles of attack which give a zero moment while holding the windward angle constant. Plot A of Figure 4.11 reveals a possible critical angle of attack where the system changes behavior due to the effect of different flow behavior.

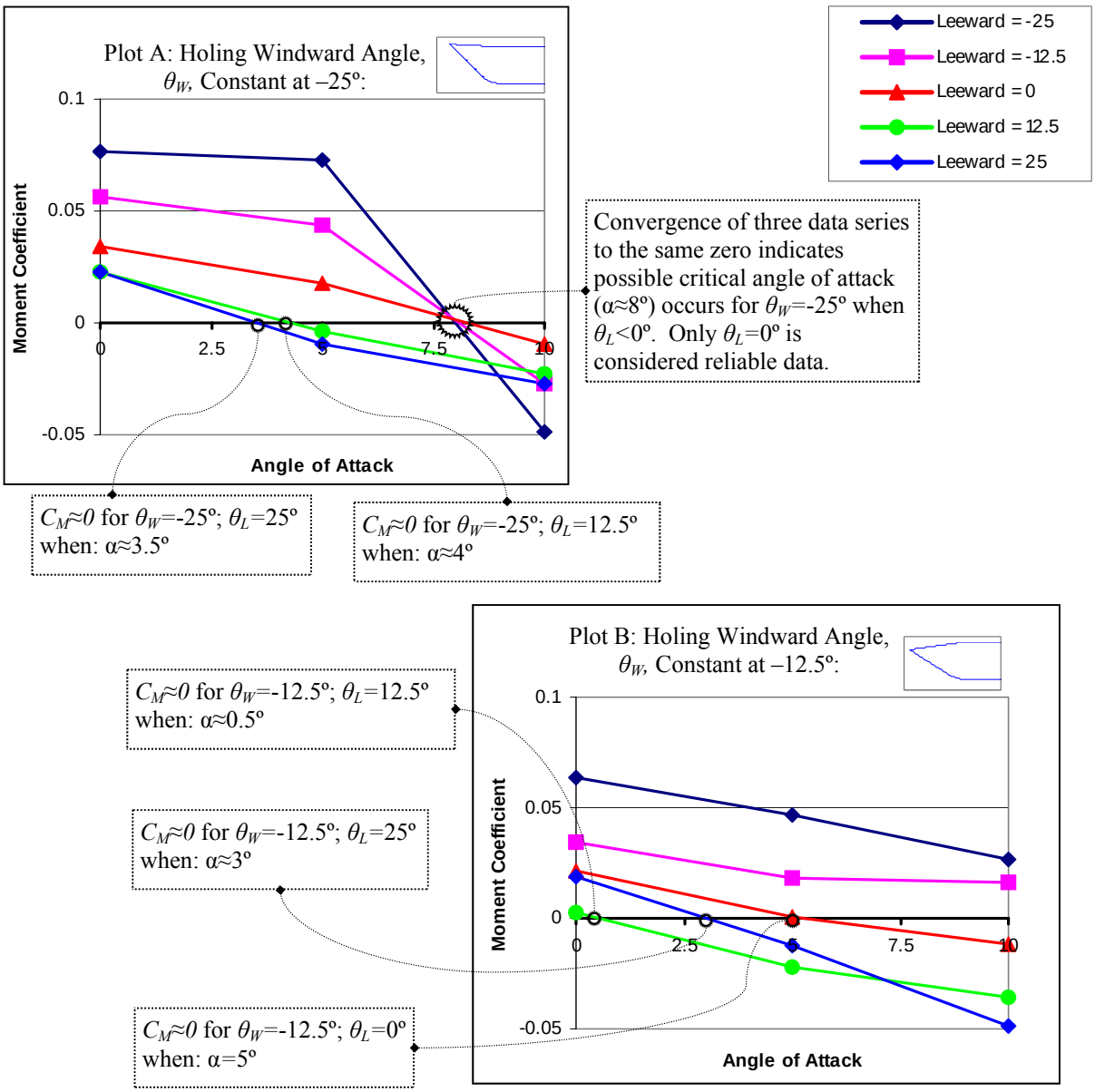

Figure 4.11: Two Plots of C_M v. α for each θ_L holding θ_W constant

Unlike the plots presented in Figures 4.9 and 4.10, switching which of the two flap angles is used to categorize the data (ie. holding θ_L constant and not θ_W) does not produce any new zero values. Of the 25 tested configurations, Table 4.3 presents which of these appear to produce a zero moment coefficient value and for what angle of attack this

would occur. The two data points representing different flow behavior, as presented in Plot A of Figure 4.11, have been eliminated.

Table 4.3: Configurations for Control Flaps and associated Angles of Attack Producing Zero Moment

Angle of Attack, α	Windward Flap Deflection Angle, θ_W	Leeward Flap Deflection Angle, θ_L
0.5	-12.5	12.5
2.5	0	-12.5
3	-12.5	25
3	12.5	-25
3.5	-25	25
5	-12.5	0
7	0	-25
8	-25	0

The data points that show a difference in the trend of the data, as mentioned above, occur for two specific cases when the angle of attack is 10º and the windward angle is -25º. It is possible that under these conditions, a bubble develops in the flow near the leading edge as shown schematically in Figure 4.12. This change in the flow characteristic leads to C_M values that do not follow the same trend as observed in all other tested cases. Further experimentation is required to verify this variation.

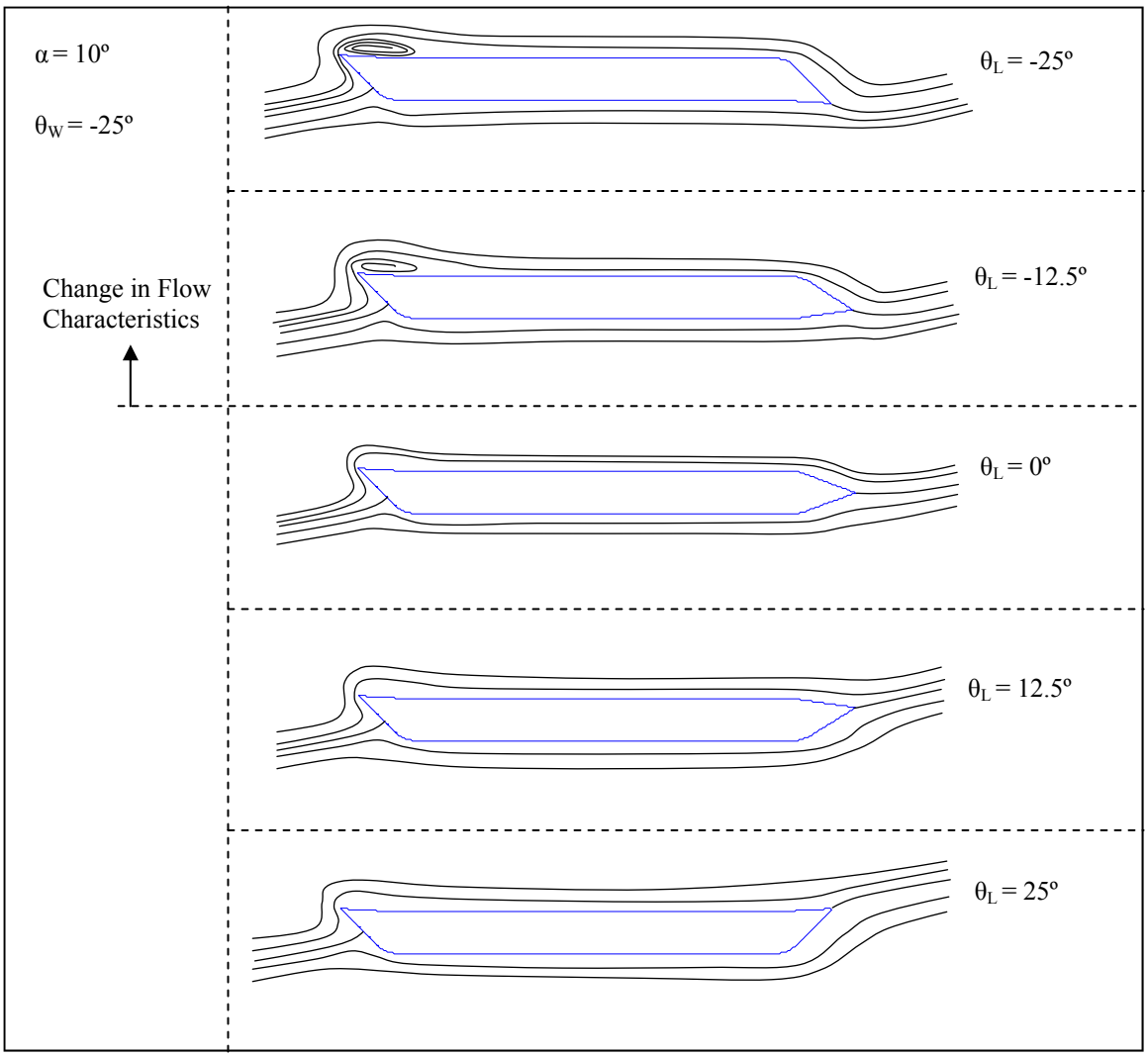

Figure 4.12: For α=10º, when θ_W=-25º, two configurations with inconsistent flow behavior: θ_L=-25º and θ_L=-12.5º

Tables 4.1 through 4.3 represent configurations for which the DVM bridge code predicts the mean moment coefficient will be zero for non-zero angles of attack. When $\alpha=0^o$, the neutral configuration can always be used; therefore, significant results develop only from values of α other than zero. Although there appears to be several promising orientations of θ_W and θ_L which predict such results, the optimal control law would require the least amount of movement of the two flaps when the wind changes orientation. This can be achieved if there is a certain range of θ_W and θ_L which yield several zero moment configurations for non-zero angles of attack. From Figures 4.10 and 4.11, it would

appear that a group of configurations develops in this manner when θ_W=*-12.5º* as well as the cases for θ_L=*-12.5º*. Consequently, the DVM code is once again implemented, here to develop more precise estimates of the moment minimizing configurations.

Figure 4.13 presents both the original moment versus θ_L plot when θ_W=*-12.5º* and an updated plot with data points for θ_L=*-7º* and θ_L=*-5º* when α=*10º*. When α=*5º*, the configuration θ_W=*-12.5º* and θ_L=*0º* gives a C_M value whose magnitude is sufficiently close to zero. The two new data points for the case when α=*10º* narrows the range over which a change in the sign of C_M occurs from 12.5º to 2º.

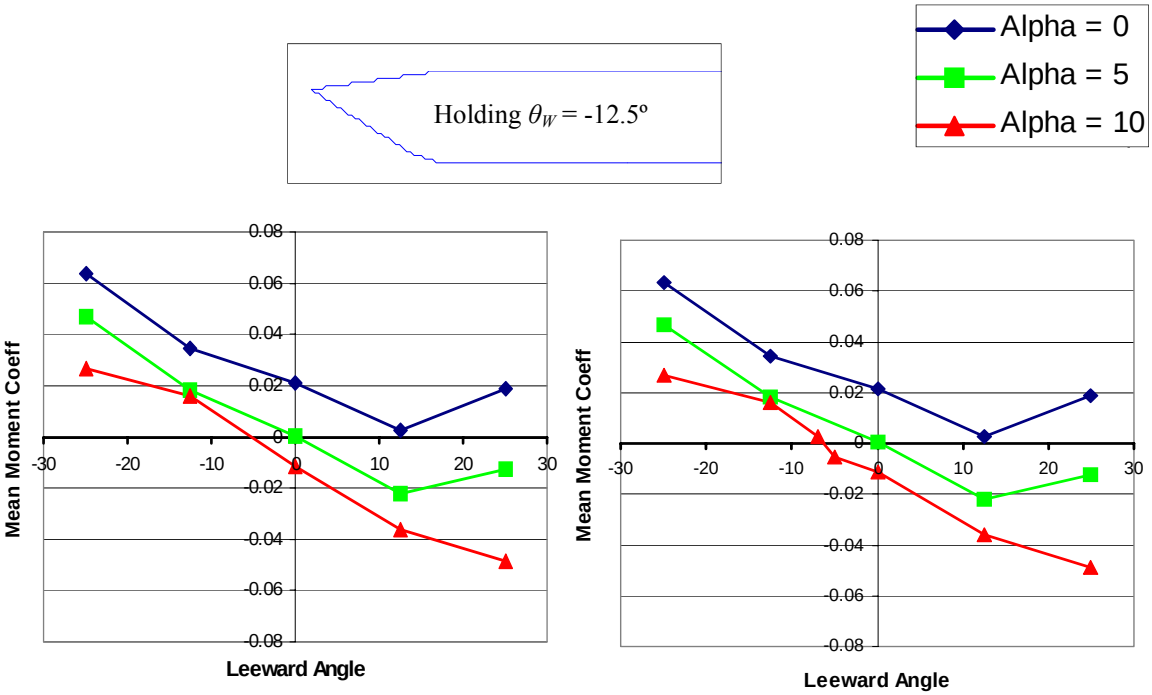

Plot A: Original Five Leeward Angles

Plot B: Updated Plot: two new Leeward Angles for α=*10º*

Figure 4.13: Original and Updated C_M v. θ_L plots for the cases when θ_W=*-12.5º*

A second promising group of configurations occurs when the leeward angle is held constant at -12.5º. Both the α=*5º* and α=*10º* data sets predict a change in sign of C_M for configurations not initially tested. Consequently, data points are tested for θ_W=*-5º* and

θ_W=*-4°*, narrowing the zero crossing to one degree for a five degree angle of attack. When α=*10°*, windward angles of -8 and -6 yield similar results. Additionally, the data point for θ_W=*-25°* and θ_L=*-12.5°*, which suggests stall behavior, is removed for the updated Plot B of Figure 4.14.

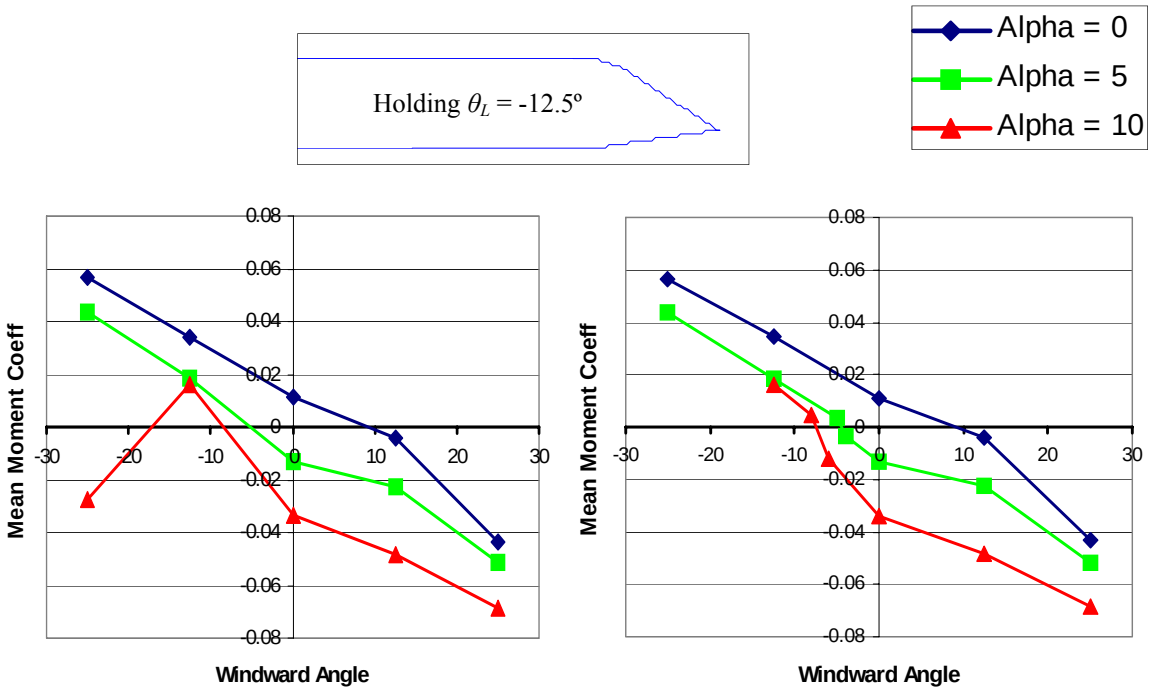

Plot A: Original Five Windward Angles

Plot B: Updated Plot: two new Windward Angles for α=*5°* and α=*10°*; unreliable data removed

Figure 4.14: Original and Updated C_M v. θ_W plots for the cases when θ_L=*-12.5°*

Figure 4.11 suggests that of the 25 original configurations, several of them will produce a zero moment coefficient for certain angles of attack. Therefore, three such configurations are tested, and all produce approximate zeros for α ranging from 2.5° to 3°, as shown in Figure 4.15.

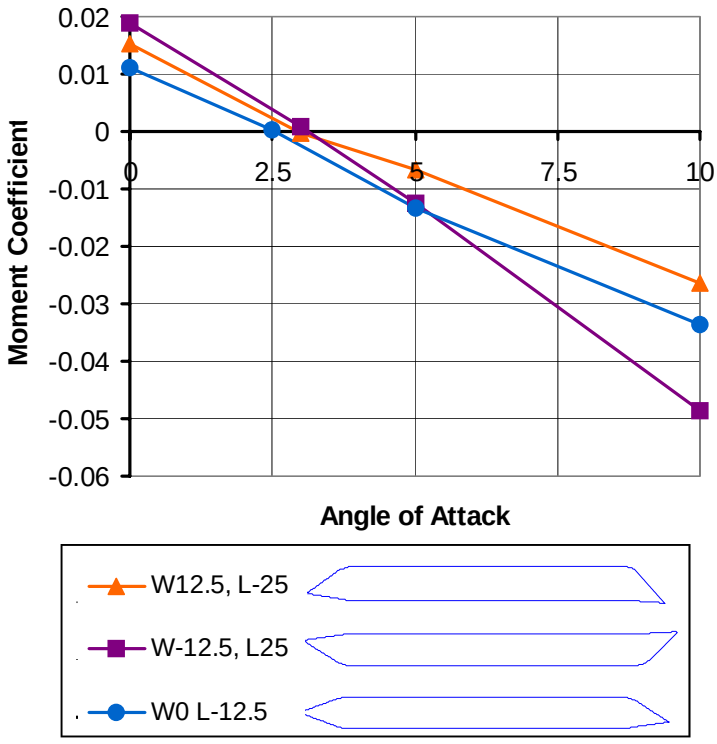

Figure 4.15: C_M v. α for three key configurations

Figures 4.16 through 4.18 are presented as a summary of the results found using the DVM code when applied to the bridge cross-section. The leeward flap angles, θ_L, are plotted against the windward flap angles, θ_W; the magnitude of the C_M values are indicated by the size of the circles, the shade of which indicates the sense of the moment. Figure 4.16 shows all C_M values calculated for zero angles of attack; the combination of θ_W and θ_L is represented by the center of each circle. In order to indicate the relative magnitude of the circles, two points are highlighted, and their C_M values are labeled. It can be seen that as the coordinates approach the dashed line, the magnitude of C_M decreases. Consequently, this line represents a contour for which combinations of θ_W and θ_L will sufficiently minimize the cross-sectional moment when $\alpha=0^o$.

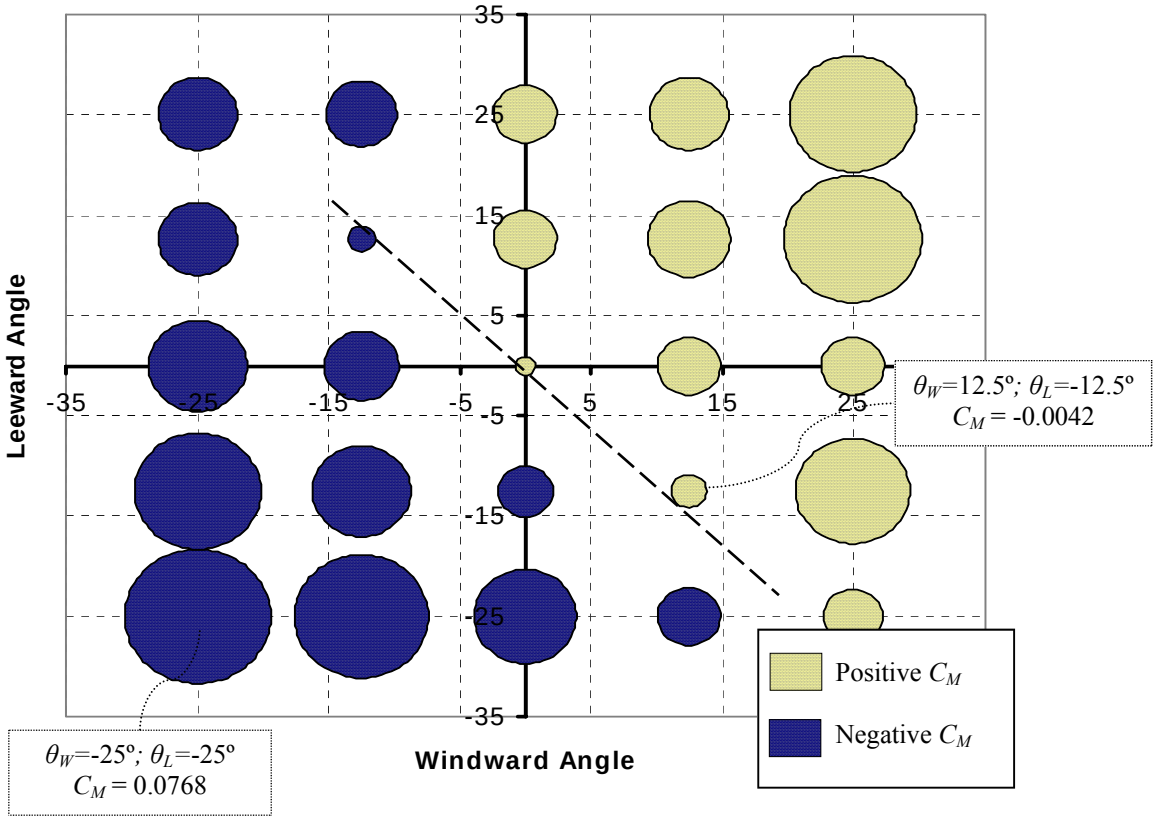

Figure 4.16: Control Relationships for $\alpha=0^o$

When α is increased to 5º, the contour line shifts both down and left, and begins to develop negative curvature. This behavior can be seen in Figure 4.17, the control law plot for $\alpha=5^o$. Based on the configurations tested, the most reliable configurations to use in conjunction with a control law are shown by the range of the dashed line. Again, the largest magnitude moment coefficient values fall in the upper right and lower left corners of the figure, confirming the gradient suggested by the shape of the dashed line.

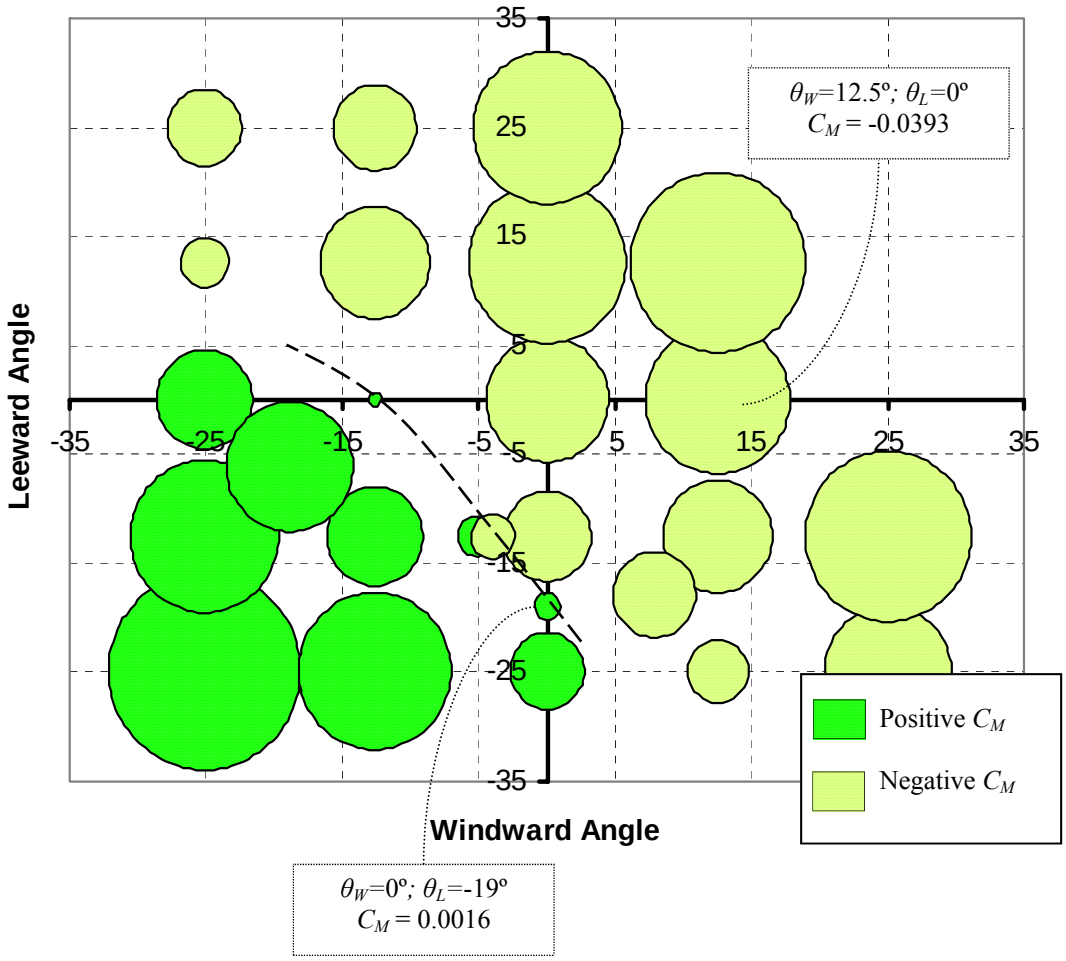

Figure 4.17: Control Relationships for $\alpha=5^o$

The final control law plot, for $\alpha=10^o$, follows the same trends suggested by Figures 4.17 and 4.17. The contour line of Figure 4.18 is shifted further left and down from the line of Figure 4.17, again with a higher degree of concavity. The negative C_M values predicted by the two cases θ_W=-25º, θ_L=-25º and θ_W=-25º, θ_L=-12.5º would drastically contradict the trends suggested by Figures 4.15 through 4.17. This reinforces the idea that the flow behavior changes with these configurations. For this reason, these two points were not included in the figure.

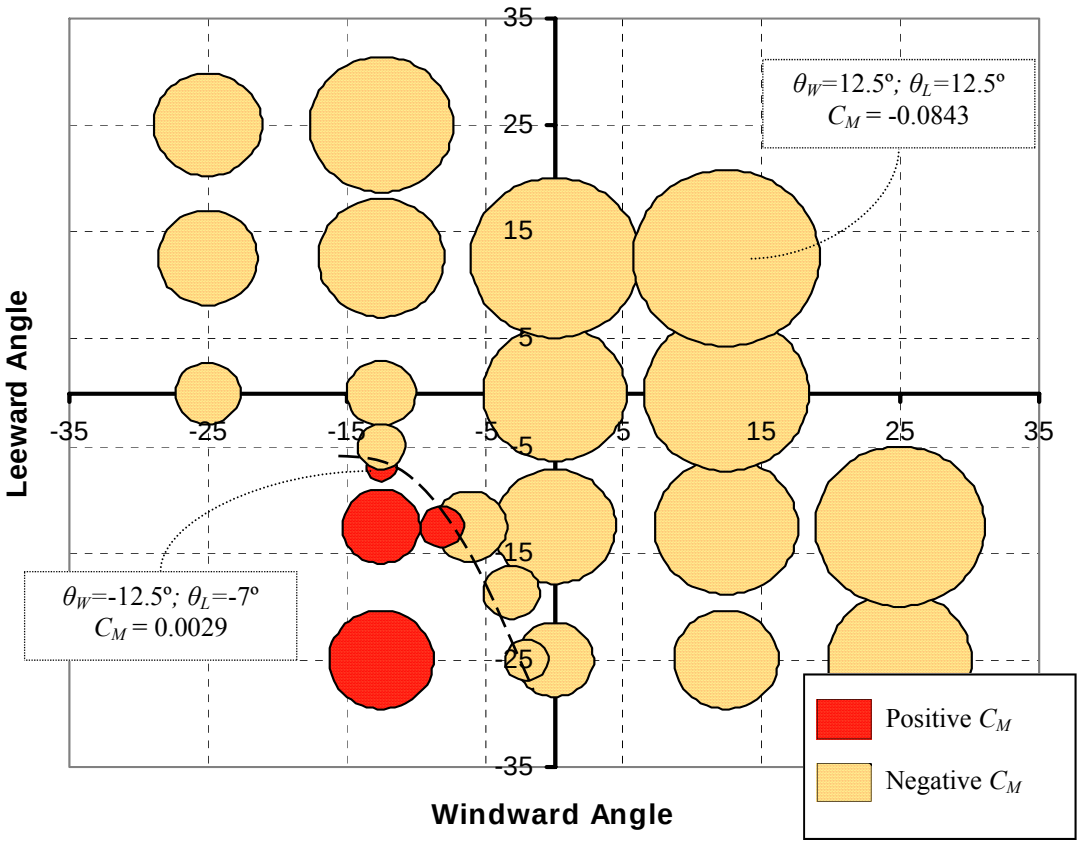

Figure 4.18: Control Relationships for $\alpha=10^{o}$

The passive control system which is developed from the data presented in this chapter can be defined in terms of the three contour lines on Figures 4.16 through 4.18. Figure 4.19 compiles these results onto one plot which demonstrates the reliable moment minimizing configurations for the three angles of attack. The dashed arrow indicates the progression from $\alpha=0^{o}$ to $\alpha=10^{o}$. Given the similarities between the three contour lines, configurations can be deduced that would minimize C_M for angles of attack other than the three specific values tested.

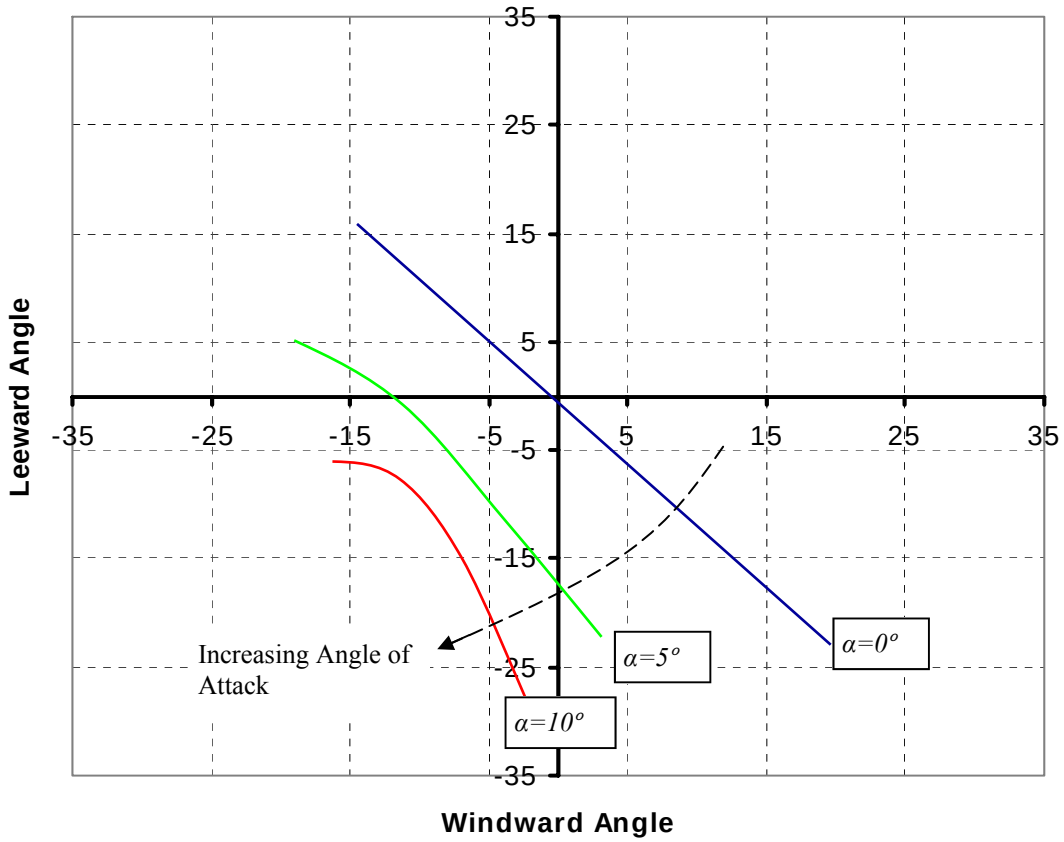

Figure 4.19: Summary of the Passive Control Relationships
Derived from the Computational Experiment

The calculations from this section, summarized in Figure 4.19, represent a foundation for future analysis. These results should be verified with wind tunnel tests of the same geometries, for instance, to see how consistent the C_M values remain. Additionally, the control relationships can be refined through an unsteady DVM technique: the angle of attack can be varied transiently as well as the orientations of the flaps.

Chapter 5

Conclusions

The two applications of the Discrete Vortex Method presented in this work show that the DVM is a useful tool for calculating wind loads over common wind engineering structures. The code developed by Qin, et al. (2001) for a surface-mounted prism, did not produce the expected behavior on the trailing wall of the prism. The version of the code presented in this thesis improves upon these results; however, the pressure distribution calculated leaves some areas for improvement. Parallel processing is proposed as a feasible solution to these problems. Because the principle of superposition holds while calculating the velocity field with the DVM, the code is especially well equipped to be parallelized.

The cross-sectional moments calculated over the proposed bridge-flap system indicated that it is possible to significantly affect the aerodynamic forces produced by a wind flow. The distinctive relationship between the three contour lines not only points to the relevance of the angle of attack, but also the success of the proposed flap design. Providing a foundation, these results should be validated using wind tunnel analysis. Other possible future areas of research leading from these results can include developing a transient analysis technique, as opposed to the quasi-steady paradigm used here. A slightly more distant goal may be extending the geometry into the third-dimension; the flaps can be implemented at various locations along the bridge length to minimize the moment coefficient at locations of interest along the length of the bridge.

Sources

Barba, L. A., et al. Advances in viscous vortex methods—meshless spatial adaption based on radial basis function interpolation, *International Journal of Numerical Methods in Fluids*, Vol. 47, 2005, pp. 387-421.

Barre, C. and Barnard, G. High Reynolds number simulation techniques and their application to shaped structures model test, *Proceedings of First IAWE Eurpoean and African Regional Conference*. Guensey, UK, 1993, pp. 83-93.

Durbin, P. A. and Pettersson Reif, B. A. *Statistical Theory and Modeling for Turbulent Flows*. John Wiley & Sons, Chichester: 2001.

Elsayed M. A. K., Elokda Y. M., Ragab S. A., Hajj M. R. Numerical Simulation of wind loads on structures and effects of incident turbulence, *Fourth European African Conference on Wind Engineering*. Prague, Check Republic 11-14 July 2005.

Homescu, C., et al. Suppression of vortex shedding for flow around a circular cylinder using optimal control, *International Journal for Numerical Methods in Fluids*, 2002. Vol. 38, pp. 43-69.

Hwang, R. R., et al. Numerical Study of Turbulent flow over two-dimensional surface-mounted ribs in a channel, *International Journal for Numerical Methods in Fluids*, 1999. Vol. 31, pp. 767-785.

Jaeger, M. and Dhatt, G. An Extended k-ε Finite Element Model, *International Journal of Numerical Methods for Fluids*, 1992. Vol. 14, pp. 1325-1345.

Jurado, J. A. and Hernandez, V. Theories of Aerodynamic Forces on Decks of Long-Span Bridges, *Journal of Bridge Engineering*. Vol. 5, February 2000, pp. 8-13.

Kobayashi, H. and Nagaoka, H. Active Control of Flutter of a Suspension Bridge, *Journal of Wind Engineering and Industrial Aerodynamics*, 1992, pp. 143-151.

Kuroda, S. Numerical Computation of Turbulent Flows, *Computational Methods of Applied Mechanical Engineering*, Vol. 3, 1974, pp. 269-289.

Kwon, S.D., et al. Active suppression in long span bridges by a passive bridge deck-flaps control system, *Wind Engineering into the 21st Century*. Vol. 2, June 1999, A. Larsen, ed. pp. 941-946.

Larsen, A. Advances in aeroelastic analysis of suspension and cable-stayed bridges, *Journal of Wind Engineering and Industrial Aerodynamics*, 1998, pp. 73-90.

Launder, B. E. and Spalding, D. B. The Numerical Computation of Turbulent Flows, *Computational Methods of Applied Mechanical Engineering*. Vol. 3, 1974, pp. 269-289.

Librescu, L. Active Aeroelastic Control of 2-D Wing-Flap Systems in an Incompressible Flowfield, *44th AIAA/ASME/ASCE/AHS/ASC Structures, Structural Dynamics, and Materials Conference*, Norfolk, VA, 7-10 April 2003.

Matsuda, K, et al. An investigation of Reynolds Number effects on the steady and unsteady aerodynamic forces on a 1:10 scale bridge deck section model, *Wind Engineering into the 21st Century*, Vol. 2: June 1999, A. Larsen, ed. pp. 971-978.

Meirovitch, L. and Ghosh, D. Control of Flutter in Bridges, *Journal of Engineering Mechanics*. Vol. 113, No. 5, May 1987, pp. 720-735.

Menter, F. R. Two-Equation Eddy-Viscosity Turbulence Models for Engineering Applications, *AIAA Journal*. Vol. 32, No. 8, 1994, pp. 1598-1605.

Munson, B.R., Young, D. F., and Okiishi, T. H. *Fundamentals of Fluid Mechanics*, 4th ed. John Wiley & Sons, New York: 2002.

Omenzetter, P., et al. Flutter suppression in long span bridges by a passive bridge deck-flaps control system, *Wind Engineering into the 21st Century*, Vol. 2: June 1999, A. Larsen, ed. pp. 1013-1018.

Qin, L., Masters Thesis, Hajj, M., Vorticity modeling for the flow over surface-mounted prism, *Department of Engineering Science and Mechanics*, Virginia Polytechnic Institute and State University, 2001.

Qin, L., Hajj, M.R., and Mook, D.T. Vorticity Modeling of the flow over a surface-mounted prism, *Third European and African Conference on Wind Engineering*. Eindhoven, the Netherlands 2-6 July 2001.

Ricciardelli, F. et al. Characteristics of the Wind-induced Forces on Long-Span Bridge Deck Sections, *Proceedings of Third European and African Conference on Wind Engineering*. Eindhoven, the Netherlands 2-6 July 2001, pp. 619-626.

Schewe, G. and Larson, A. Reynolds number effects in the flow around bluff bridge deck cross sections, *Proceedings of Second IAWE European and African Regional Conference*. Genova, Italy, 1997.

Scruton, C. Experimental investigation of aerodynamic stability of suspension bridge with special reference to seven bridges, *Proceedings of the Fifth Civil Engineering Conference*. 1 Part 1, No. 2, 1952, pp. 189-222.

Sung, H. J., et al. Vortex simulation of leading-edge separation bubble with local forcing, *Fluid Dynamics Research*, 1996. Vol. 18, pp. 99-115.

Taylor, I. and Vezza, M. Aeroelastic stability analysis of a bridge deck with added vanes using a discrete vortex method, *Journal of Wind and Structures*, 2002. Vol. 5, pp. 277-290.

Taylor, I. and Vezza, M. Calculation of the flow field around a square section cylinder undergoing forced transverse oscillations using a discrete vortex method, *Journal of Wind Engineering and Industrial Aerodynamics*, 1999. Vol. 82, pp. 271-291.

Taylor, I. and Vezza, M. Prediction of unsteady flow around square and rectangular section cylinders using a discrete vortex method, *Journal of Wind Engineering and Industrial Aerodynamics*, 1999. Vol. 82, pp. 247-269.

Tutar, M. and Oguz, G. Large eddy simulation of wind flow around parallel buildings with varying configurations, *Fluid Dynamics Research*, 2002. Vol. 31, pp. 289-315.

Vezza, M. Flow Control on Bridge Decks Using a Discrete Vortex Method, *Eleventh International Conference on Wind Engineering*, Lubbock, TX: 2-5 June 2003.

Wagner, G. J. and Liu, W. K. Turbulence simulation and multiple scale subgrid models, *Computational Mechanics*, 2000. Vol. 25, pp. 117-136.

Wilcox, D. C. Multiscale model for turbulent flows, *AIAA Journal*, Vol. 26, Nov. 1988, pp. 1311-1320.

Wilde, Krzysztof, et. al., Suppression of Bridge Flutter by Active Deck-Flaps Control System, *Journal of Engineering Mechanics*, Vol. 127, No. 1: January 2001, pp. 80-89.

Wright, Nigel. Appropriate use of computational wind engineering, *Structures 2004, Building on the Past: Securing the Future*. Structures Congress 2004. George E. Blandford, ed. 22-26 May 2004, Nashville, Tennessee, USA.

Xu, Y. L. Buffeting of Tsing Ma Suspension Bridge: Analysis and comparison *Wind Engineering into the 21st Century*, Vol. 2, June 1999, A. Larsen, ed. pp. 1081-1088.